

THESIS FOR THE DEGREE OF DOCTOR OF PHILOSOPHY

**Retrieval of ocean surface winds and currents using
satellite synthetic aperture radar
and infrared radiometry**

GISELA KARINA CARVAJAL



CHALMERS

Department of Earth and Space Sciences
CHALMERS UNIVERSITY OF TECHNOLOGY
Gothenburg, Sweden, 2013

Retrieval of ocean surface winds and currents using satellite synthetic aperture radar and infrared radiometry

GISELA KARINA CARVAJAL

ISBN 978-91-7385-928-8

©GISELA KARINA CARVAJAL, 2013.

Doktorsavhandlingar vid Chalmers tekniska högskola

Ny serie Nr 3609

ISSN: 0346-718X

Department of Earth and Space Sciences

Radar Remote Sensing Group

Chalmers University of Technology

SE-412 96 Gothenburg, Sweden

Telephone + 46 (0)31-772 1000

Cover: Left: Map for surface winds in the Amundsen Sea, Antarctica, on April 3 2010 at 08:35 UTC. The dashed line represents the limits of the ice coverage. The wind map was obtained from an image acquired by the ASAR sensor using the CMOD-IFR2 geophysical model function. The wind directions were obtained from the ERA-interim model. Right: Map of surface currents in the Baltic Sea on June 29 2011 between 09:03 and 12:22 UTC. The surface currents were derived with the maximum cross correlation method applied to two images from AVHRR/3 sensors.

Printed by Chalmers Reproservice
Chalmers University of Technology
Gothenburg, Sweden 2013

Retrieval of ocean surface winds and currents using satellite synthetic aperture radar and infrared radiometry

GISELA KARINA CARVAJAL

Department of Earth and Space Sciences

Chalmers University of Technology

Abstract

This thesis focuses on the development, analysis and evaluation of methods for the retrieval of ocean surface winds with synthetic aperture radar (SAR) and surface currents with infrared (IR) radiometer sensors.

The SAR wind speed retrievals are based on geophysical model functions using wind directions obtained with two approaches. The first approach determines wind directions from the spatial detection of image features. This method detects small-scale variations in the wind directions. This work includes a validation against in-situ data and an assessment of the retrievals at different resolutions with respect to wind data from a scatterometer sensor and a weather prediction model (WPM). The assessment results show that the detection of small-scale wind features is improved by using the wind direction retrievals from the SAR data. In polar regions, however, the approach is limited by the stability of the marine atmospheric boundary layer, which results in a lack of features for the wind direction retrieval. Thus, the second approach uses wind directions from a WPM to produce wind maps of the Amundsen Sea in Antarctica. Time series of wind maps from both SAR and WPM data were correlated with components of the deep water velocities measured by an acoustic Doppler current profiler at 72.5°S and 116.3°W during 2010 and 2011. This evaluation showed that the SAR wind data have correlations up to $R_{SAR} = 0.71$, with larger statistical significance than wind data from a WPM ($R_{WPM} = 0.41$). Thus, SAR surface winds can be highly correlated with variations in the warm deep water currents, which in previous studies has been shown to be related to the basal melting of the ice shelves in the Amundsen Sea.

A method for surface current retrieval with IR sensors was developed from the maximum cross correlation (MCC) technique, which correlates two IR images of the same region acquired at different times and assumes that the current field is produced by the horizontal advection of surface temperatures measured by the IR sensors. The method was evaluated in cloud free days and was qualitatively compared with surface current data from a WPM. The results show that the MCC retrievals are largely in agreement with the modeled currents for 3 h of time delay between the IR images. However, for longer time delays (6 to 10 h), the agreement of the current fields depreciates.

In summary, this work resulted in the development and quality assessment of algorithms

for the retrieval of ocean surface winds and currents from satellite data with possible uses in meteorological and oceanographic applications.

Keywords: surface winds, wind direction, synthetic-aperture radar, surface currents, infrared radiometry, maximum cross correlation.

List of appended papers

This thesis is based of the work described in the following papers:

- I. Carvajal, G.K., Eriksson, L.E.B., and Ulander, L.M.H., “Retrieval and quality assessment of wind velocity vectors on the ocean with C-band SAR”, accepted for publication in *IEEE Transactions on Geoscience and Remote Sensing*.
- II. Wåhlin, A., Kalén, O., Arnborg, L., Björk, G., Carvajal, G.K., Ha, H., Kim, T., Lee, S., Lee, J., and Stranne, C., “Variability of warm deep water inflow in a submarine trough on the Amundsen Sea shelf”, accepted for publication in *Journal of Physical Oceanography*.
- III. Carvajal, G.K., Wåhlin, A., Eriksson, L.E.B., and Ulander, L.M.H., “Correlation between synthetic aperture radar surface winds and deep water velocity in the Amundsen Sea, Antarctica”, *Remote Sensing*, vol. 5 no. 8, pp. 4088-4106, 2013.
- IV. Carvajal, G.K., Eriksson, L.E.B., Ulander, L.M.H. and Berg, A., “Comparison between current fields detected with infrared radiometry and modeled currents around Sweden”, accepted for publication in *Proc. IEEE International Geoscience and Remote Sensing Symposium (IGARSS)*, Melbourne, Australia, July 21-26, 2013.

Other publications (not appended)

Besides the appended papers, the author has contributed to the following publications. They are listed for completeness but have not been appended since they represent an early stage of the research presented in this thesis, consist of partially overlapping material, or are research papers done previous to the Doctoral studies.

1. Johansson, A. M, Eriksson, L.E.B., Hassellöv, I., Landquist, H., Berg, A., and Carvajal, G., “Remote sensing for risk analysis of oil spills in the Arctic Ocean”, accepted for publication in *Proc. ESA Living Planet Symposium*, Edinburgh, UK, September 9-13, 2013.
2. Carvajal, G., “Retrieval of wind velocity vectors over the ocean surface with spaceborne synthetic aperture radar: Implementation and quality assessment”, Technical report No. 6, Department of Earth and Space Sciences, Chalmers University of Technology, March, 2011.
3. Carvajal, G., Eriksson, L.E.B., and Ulander, L.M.H., “Retrieval and assessment of sub-mesoscale wind velocity vectors with synthetic aperture radar”, in *Proc. International Geoscience and Remote Sensing Symposium (IGARSS)*, Vancouver, Canada, July 24-29, pp. 2041-2044, 2011.
4. Carvajal, G., Eriksson, L.E.B., Kononov, A., and Dokken, S., “Operational retrieval of sea surface dynamics from SAR data for safety and security”, in *Proc. Third International Workshop SeaSAR*, 25-29 January 2010, Frascati, Italy, ESA SP-679, 2010.
5. Carvajal, G. K., Duque, D. J., and Zozaya, A. J., “RCS estimation of 3D metallic targets using the moment method and Rao-Wilton-Glisson basis functions”, *Applied Computational Electromagnetics Society Journal*, vol. 24 no. 5, pp. 487-492, 2009.
6. Carvajal, G., Penna, B., and Magli, E., “Unified lossy and near-lossless hyperspectral image compression based on JPEG 2000”, *IEEE Geoscience and Remote Sensing Letters* vol. 5 no. 4, pp. 593-597, 2008.

Contents

Abstract	iii
List of appended papers	v
Other publications	vii
Contents	ix
1 Introduction	1
2 Sensors used in satellite oceanography	5
2.1 Active sensors	5
2.1.1 Synthetic aperture radar	6
2.1.2 Scatterometer	9
2.1.3 Other active sensors	11
2.2 Passive sensors	12
2.2.1 Infrared Radiometer	12
2.2.2 Other passive sensors	13
3 Surface wind retrieval from synthetic aperture radar	15
3.1 Backscatter properties of the ocean surface	16
3.2 Wind speed from geophysical model functions	18
3.3 Wind direction from SAR image streaks	21
3.4 Computation of surface winds	26
3.5 Reference data	27
3.5.1 In-situ sensors	27
3.5.2 ASCAT scatterometer	29
3.5.3 Weather prediction models	29

4	An application of surface winds for oceanography in Antarctica	33
4.1	Review of key concepts on ocean circulation	34
4.1.1	Ekman transport	34
4.1.2	Barotropic and baroclinic conditions	35
4.1.3	Upwelling and downwelling	36
4.2	Factors affecting the deep currents circulation	37
4.2.1	Temperature and salinity	37
4.2.2	Upslope benthic Ekman transport	38
4.2.3	Surface wind	39
4.3	Correlation between surface winds and deep currents	39
4.3.1	Data	39
4.3.2	Method	40
4.4	Results	41
5	Surface current retrieval from infrared radiometry	43
5.1	Brightness temperature of the ocean surface	44
5.2	Maximum cross correlation method	45
5.3	Data	47
5.3.1	AVHRR	47
5.3.2	HIROM-B	47
5.4	MCC evaluation	47
6	Conclusions and outlook	49
	Acknowledgements	51
	Bibliography	53

Introduction

Oceans and climate are inextricably linked as oceans play a fundamental role in mitigating climate change by serving as a major heat and carbon sink [1–3]. Human activities related to oceans include maritime transport, which accounts for 90% of international trade with more than 100,000 commercial ships worldwide; energy development (e.g. conversion of tidal, wave, thermal and wind energy); exploration and extraction of oil, gas, gravel, sand and mineral mining from the coast to deep water; fishing and aquaculture; and disposal of waste from land (e.g. sewage, non-point sources, carbon dioxide sink). These activities require a regular monitoring of the oceans in order to observe and predict ocean acidification, sea level increase, and changes in water temperature and currents, all of which in turn impact the health of marine species, ecosystems, and coastal communities throughout the world [3–6].

The large scale three dimensional ocean circulation and the formation of water masses create pathways for the transport of heat, freshwater and dissolved gases such as carbon dioxide from the surface ocean into a density stratified deeper ocean [3]. To gain increased knowledge about this complex system, monitoring of numerous variables is required. According to the Ocean Observations Panel for Climate (OOPC) oceanic observations are currently feasible in the following essential climate variables (ECV) [7]: 1) Surface atmosphere: air temperature, precipitation, evaporation, sea level pressure, surface radiation budget, surface winds (speed and direction), surface wind stress, water vapor; 2) Ocean surface: sea surface temperature, sea surface salinity, sea level, sea state, sea ice, ocean current, ocean color, carbon dioxide partial pressure; 3) Ocean subsurface: temperature, salinity, ocean current, nutrients, carbon, ocean tracers, phytoplankton.

This thesis contributes to the applicability of remote sensing data for the study of the ocean. For this, it focuses on two of the mentioned ECV: surface winds and ocean currents.

Wind is moving air. As air molecules are dragged across the sea surface, they collide with water molecules creating a pressure gradient. The energy transfer by frictional drag, if prolonged, raises waves and generates currents. Surface drag, momentum exchanges, fluxes of

sensible heat and moisture also depend on the wind speed. Thus, the surface wind field is a sensitive measure of the state of the global coupled climate system and is valuable for climate change and climate model evaluation [7].

Ocean currents are the central core of dynamical oceanography. It is the overall movement of the ocean which transports heat poleward from the low latitudes and contributes to the control of Earth's climate and which tends to exert a stabilizing influence upon long term climatic fluctuations of the atmosphere. Besides the wind, at global scale, the circulation is also governed by the distribution of water masses with different temperature and salinity, the Coriolis effect, and tides caused by the gravitational pull of the Moon and the Sun. Also, depth contours, shoreline configurations and interaction with other currents influence a current's direction and strength.

The use of Earth orbiting satellites as platforms for ocean viewing sensors offers the opportunity to achieve wide synoptic coverage at fine spatial detail and a repeated regular sampling to produce time series of data [8–10]. Because of this, the methods developed in this thesis use data acquired by satellite-borne sensors.

For surface winds, an algorithm to retrieve wind direction and speed from satellite synthetic-aperture radar (SAR) data has been developed, evaluated and addressed in terms of quality and limitations. SAR data have been used since it allows to determine wind information at higher resolution than most of the commonly used sensors for surface wind. Furthermore, wind data have been used to study deep water ECV. For surface currents, an algorithm for the retrieval of current fields with satellite infrared (IR) radiometry data has been implemented and a first comparison has been conducted with data from a weather model.

The main objectives of this thesis include: 1) the study, development and implementation of methods for retrieval of surface winds with SAR and surface currents from IR; 2) the evaluation and assessment of those methods with respect to other data sources; 3) the evaluation of the relationship of surface winds with deep water ECV.

The main work of this thesis is included in the following papers:

Paper A “Retrieval and quality assessment of wind velocity vectors on the ocean with C-band SAR”, presents the implementation of a wind retrieval algorithm for C-band SAR, compares its performance at 5 km resolution with respect to in-situ measurements, and at 5, 10 and 20 km resolution with wind data from a scatterometer and a numerical weather model. A significant contribution of this work is to assess the difference between the SAR wind retrievals and other wind sources at different resolutions.

Paper B “Variability of warm deep water inflow in a submarine trough on the Amundsen Sea shelf”, presents a study of the deep water inflow in the Amundsen Sea basin during 2010 and 2011. The research was based on using measurements from an Acoustic Doppler Current Profiler (ADCP) located in the Amundsen Sea. Data from deep water velocities,

temperature and salinity were correlated with surface winds from a weather prediction model to investigate the wind as the forcing variable of the presence of warm deep waters melting the ice shelves from below. This work identifies a correlation between one of the components of the deep current velocity and the surface wind.

Paper C “Correlation between synthetic aperture radar surface winds and deep water velocity in the Amundsen Sea, Antarctica”, presents an extended analysis of the correlation between the deep water velocities registered by the ADCP of Paper B and SAR wind speed retrievals during the months with minimum ice coverage. For reference, correlations were also computed with modeled wind data. The comparison indicates an improvement in the significance of the correlations of SAR data with respect to those derived purely from the model.

Paper D “Comparison between current fields detected with infrared radiometry and modeled currents around Sweden”, presents the results from the implementation of an algorithm for the retrieval of surface currents from IR data and a comparison with estimates from a weather prediction model.

Sensors used in satellite oceanography

The satellite sensors used to measure oceanic parameters can be classified according to the nature of the received signal, the measurement method, and their frequency of operation. The broadest classification into active and passive sensors corresponds to the nature of the received signal which can either be backscattered or emitted from the ocean surface. This chapter consist of a brief review of the main sensors used in satellite oceanography, with focus on the sensors used in this thesis.

2.1 Active sensors

The active sensor most broadly used in Satellite Oceanography is radar. The term radar stands for *RAdio Detection And Ranging*. A radar is basically an electromagnetic system for the detection and location of reflecting objects [11].

The basic interaction between radar sensors and target objects is described by the radar equation [11]:

$$P_r = \underbrace{\frac{P_t G_t}{4\pi R_t^2}}_{(i)} \underbrace{\sigma}_{(ii)} \underbrace{\frac{1}{4\pi R_r^2}}_{(iii)} \underbrace{\frac{1}{L}}_{(iv)} \underbrace{A_r}_{(v)} \quad (2.1)$$

where P_t and P_r [W] represent the transmitted and the received power, G_t [dimensionless] is the gain of the transmitting antenna, R_t and R_r [m] are the distances from the transmitting and receiving antennas to the target, σ [m²] is the target's radar cross section, L [dimensionless] stands for the propagation losses in the atmosphere, and A_r [m²] is the effective area of the receiving antenna.

The factor (i) in eq. 2.1 represents the power density [W/m²] that the radar transmitter produces at a target. This power density is scattered by the target with radar cross section, σ , which has units of area [m²]. The factor (iii) represents the isotropic spreading of the scattered power from the target back to the radar receiving antenna. Thus the product (i)·(ii)·(iii)·(iv)

represents the reflected power density at the radar receiver [W/m^2]. The receiver antenna then collects this power density with effective area A_r [m^2], yielding the power received by the radar [W].

The radar cross section is an effective scattering area which can be either larger or smaller than the geometrical cross section of a target. The exception is the large (radius \gg wavelength) metallic sphere which has a radar cross section equal to its geometrical cross section. However, the radar cross section is a useful concept because it is a property of the target alone which may be measured or calculated. Thus, σ allows the performance of a radar system with a given target to be analysed independent of the radar parameters. This property is, in general, a strong function of the orientation of the radar and target, or, for the bi-static case (radar transmitter and receiver not co-located), a function of the transmitter-target and receiver-target orientations. A target's σ depends on its size, the reflectivity of its surface, the directivity of the radar reflection caused by the target's geometric shape, and the frequency and polarization of the electromagnetic signal used for its detection [11, 12].

The polarization of an electromagnetic signal is defined by the orientation of its electric field. For linear polarization, a vertical (V) or a horizontal (H) polarization implies an electric field aligned in the vertical or horizontal planes. Thus, since the emitted signal can change polarization state after interacting with the target, the backscattered signal is referred to as having a HH, HV, VH or VV polarization, reflecting the transmitted and received states.

Radar sensors can be used to measure the backscatter from the sea surface. This is quantified in terms of σ_0 , the normalised radar cross section of the ground, as [11]

$$\sigma_0 = E \left\{ \frac{\sigma}{A_s} \right\} \quad (2.2)$$

where, for an illuminated portion of the ocean surface σ [m^2] represents its radar cross section, $E\{ \}$ represents the ensemble average, A_s [m^2] is its area, and σ_0 is dimensionless, but often expressed in decibels.

2.1.1 Synthetic aperture radar

A SAR is a sensor capable of producing high resolution images of the Earth surface nearly independent of the weather conditions. The independence of weather conditions applies when using electromagnetic signals between 1 and 10 GHz, which are almost unaffected by absorption in the atmosphere.

The cross track resolution δr of SAR sensors is achieved by a modulated pulse with bandwidth B (generally achieved with a technique called pulse compression), as $\delta r = \frac{c}{2B}$ (see Fig. 2.1), with $c = 3 \times 10^8$ m/s being the speed of light [12]. This resolution projects into a ground range resolution $\delta y = \frac{c}{2B} \cdot \frac{1}{\sin \theta_i}$, with θ_i being the incidence angle in an horizontal ground

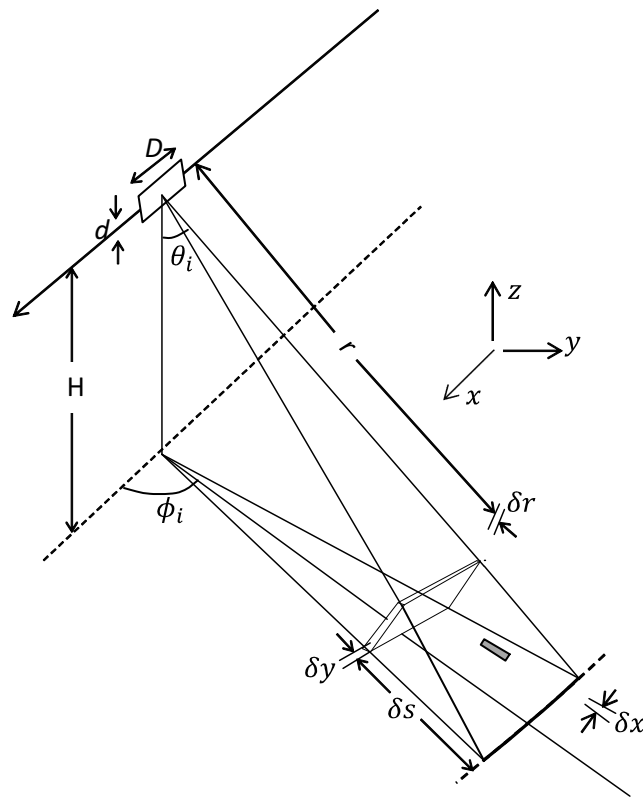


Figure 2.1: Viewing geometry of a SAR sensor. Horizontal ground geometry is assumed for simplicity.

geometry¹.

For the azimuth (along track) resolution SAR uses a principle called aperture synthesis to construct an effective antenna dimension in the direction of motion much larger than its physical dimension, hence its name. It accomplishes this by transmitting a sequence of highly repeatable, stable signals and coherently adding up the scattered returns over an integration time t_i (typically on the order of a second for satellite SAR). During this coherent integration process, the platform moves a distance $D' = v \cdot t_i$, which is the synthetic aperture length. The effective beam width is approximately the reciprocal of the synthetic aperture length in terms of half wavelengths, i.e. $2D'/\lambda$, and hence results in a significantly improved resolution in the along track direction [12–14].

The construction of a SAR image requires a coordinate system for the acquisitions in the range and azimuth directions. In the range direction the pixel positions are assigned proportional to the time delay to the ground point in question. The other coordinate is assigned according to the Doppler shift of the received signal, which is due to a combination of the platform velocity and, in the case of an orbiting satellite, the appropriate component of the Earth's surface rotational velocity. Thus, the (x, y) coordinates in the SAR image are established by locations of constant time delay and constant Doppler shift, a non-orthogonal coordinate system. It can be

¹For the satellite case the look direction in which the radar antenna is pointing is not the same as the incidence angle at the ground due to the curved Earth.

shown that the Iso-Doppler contours are defined by

$$\left(\frac{x}{H}\right)^2 \left[\left(\frac{\delta f_{D0}}{\delta f_D}\right)^2 - 1 \right] - \left(\frac{y}{H}\right)^2 = 1 \quad (2.3)$$

where δf_{D0} is the Doppler shift in frequency in the direction of the platform motion, and δf_D is the Doppler shift elsewhere.

The transmitted frequency, f_t , is Doppler shifted by the platform's motion at velocity ν by

$$\delta f_D = \frac{2f_t\nu}{c} \frac{x}{\sqrt{x^2 + y^2 + H^2}} \quad (2.4)$$

The maximum Doppler frequency comes from the direction of the positive x axis; the frequency shifts are positive in the approaching direction, negative in the receding, and zero along the direction orthogonal to the flight path. This implies that any relative motion between transmitter and target will induce a Doppler shift, which for SAR images will cause positional offsets, e.g. moving trains off tracks and moving ships away from their wakes. This phenomenon is important for understanding SAR images of the moving ocean, especially rapid propagating surface waves. A point target moving with a radial velocity component, ν_r , will be displaced from its true position by an amount Δx in the azimuth coordinate given by

$$\Delta x = \frac{r}{\nu} \nu_r \quad (2.5)$$

Satellite SAR systems in L-band (1 GHz), C-band (5 GHz) and X-band (10 GHz), have been and are currently used to investigate the ocean, revealing information about surface winds, surface currents, surface and internal waves, bathymetric features, oil spill and other parameters. These include: the L-band SAR on the early Seasat, the Japanese Earth Resources Satellite 1 (JERS-1) and more recently the Phased Array type L-band (PALSAR) sensor on the Advanced Land Observing Satellite (ALOS); the wide selection of C-band SAR sensors on the European remote sensing satellites (ERS) ERS-1 and ERS-2, Radarsat-1 and Radarsat-2, the Radar Imaging Satellite 1 (RISAT-1) and the Advanced SAR (ASAR) sensor on the Environmental Satellite (Envisat). Data from ASAR has been used for the wind retrieval evaluation in Papers A, B, and C; X-band sensors on Terrasar-X, its add-on for Digital Elevation Measurement (TanDEM-X), the CONstellation of small Satellites for the Mediterranean basin Observation (COSMO-Skymed), and the Korea Multi-Purpose Satellite-5 (KOMPSat-5).

Surface wind speed and wind direction have been related to the backscatter of the ocean surface, and independently, streak features on SAR images have been related to the wind direction. These phenomena are presented in Chapter 3, where the physical background of the relationships between SAR measurements and surface winds is described. Furthermore, it is described how these relationships are used in Papers A, B and C for the development and implementation of algorithms for surface wind retrieval using C-band SAR data. The Doppler velocity variation of eqs. (2.3) and (2.4) is used in the literature to detect information about surface currents.

For this, mainly two different techniques have been developed: the along-track interferometry (ATI), which requires two SAR antennas [15, 16], and the Doppler centroid anomaly analysis, which requires one SAR antenna [17, 18]. However, so far both techniques are restricted to the retrieval of only one component of the current field. SAR surface wave parameters include wave spectra [19, 20], significant wave height², mean wave period and wave power [22–24]. Internal waves, produced in stratified waters, have been studied in [25, 26]. Bathymetry, reflected by long swell wave refraction governed by underwater structures in shallow areas has been observed in [27, 28]. Techniques for detection of the oil spill damping of capillary waves have been proposed in [29–31].

2.1.2 Scatterometer

A scatterometer is an oblique viewing radar pointed towards the sea from an aircraft or a satellite at incidence angles normally between 20° and 70° . The receiver simply measures the backscattered power from the field of view (FOV) of the antenna beam in order to determine σ_0 . There is no attempt to preserve the phase information after demodulating the microwave signal. Therefore scatterometers do not resolve variations of σ_0 in range and azimuth in a detailed way and cannot generate high resolution images [8]. At the most basic level, as a device to measure backscatter, there is essentially little difference between a scatterometer deployed on a satellite, on an aircraft, or from a static point above the ground.

The primary function that dictates the form of a scatterometer is the requirement to measure σ_0 across a grid of relatively coarse cells (typically 25-50 km resolution for satellites). Over such wide area, the backscatter is averaged over a large number of independent scattering elements, and so an ensemble average measure of roughness is achieved, unaffected by speckle.

Scatterometers are mainly designed to measure wind speed and direction over the ocean surface. Thus, for this purpose they are designed to view the same ground patches from several directions. Figure 2.2 shows two different configurations for satellite scatterometers. For the configuration in Fig. 2.2(a), used currently by the Advanced SCATterometer (ASCAT) sensors, ASCAT-A (used for comparison in Paper A) and ASCAT-B, operating at C-band and on-board the MetOp-A/B satellites, two different swaths are observed by three different antennas with different squint angles with respect to the satellite path. Thus for each resolution cell there are three different observations. In Fig. 2.2(b) the antennas have a rotating platform from where there can be up to 4 viewing of the same resolution cell. This is used by the current Oceansat, operating at Ku-band (13.5 GHz). In both cases a measurement of σ_0 is done with:

- A particular microwave frequency, f . A scatterometer that measures at a range of frequencies is called a spectrometer, but so far they have not been implemented in satellites.

²The *significant wave height*, $\xi_{1/3}$, represents the average height of the highest one-third of all waves occurring in a particular time period [21].

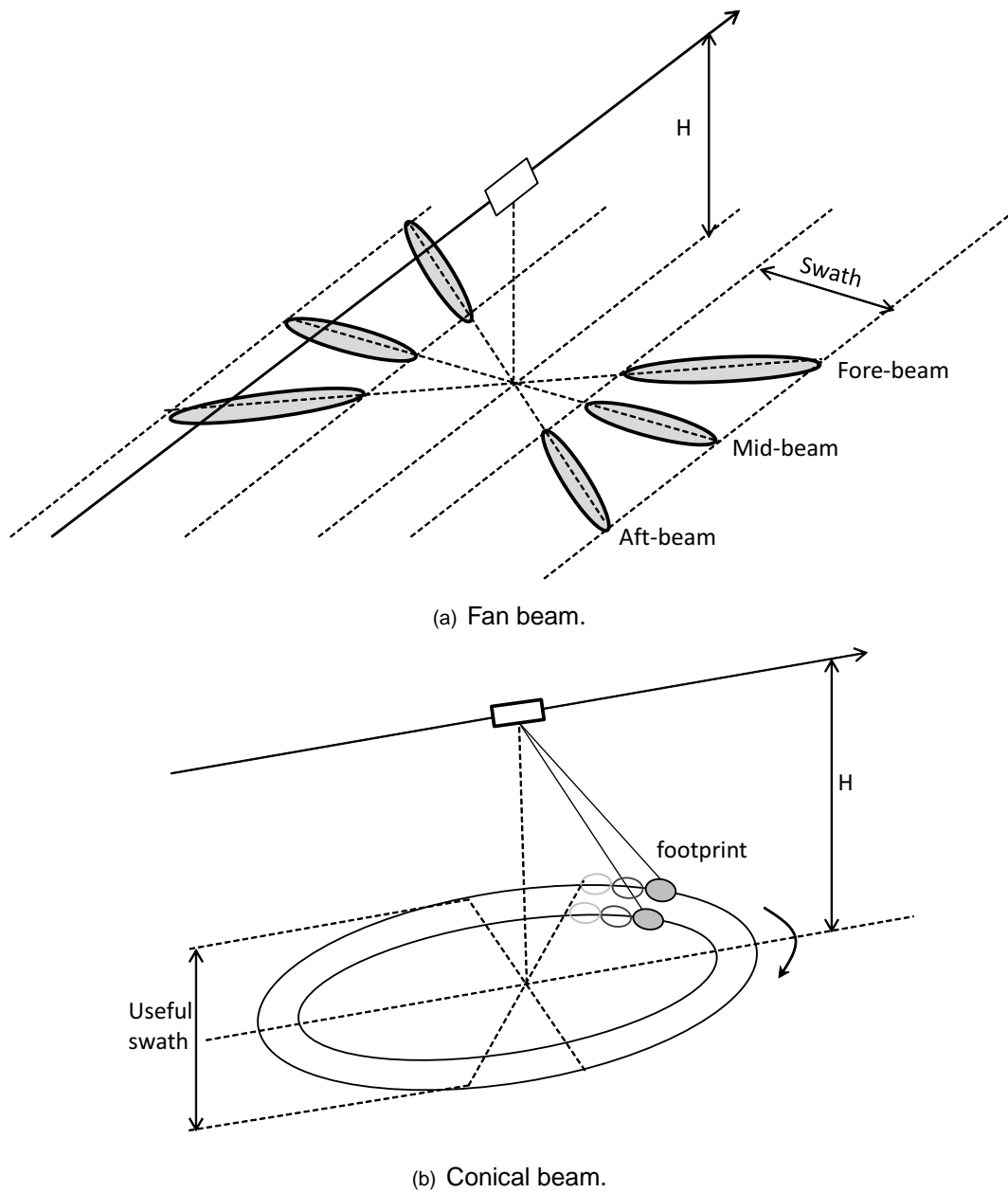


Figure 2.2: Geometries for scatterometer sensors.

- A polarization state for transmitting and receiving. The instrument may measure one or all: HH, VV, HV or VH.
- A known incidence angle, θ , which may or may not vary between the measurements depending on the instrument design.
- Two or more different azimuth orientations, ϕ , defined as the direction of the projection onto the earth surface of boresight of the radar beam, measured in relation to the geographical north. This is crucial for retrieving the wind direction information.

The resolution changes according to the geometry of the instrument. For fan beams as in Fig. 2.2(a) the azimuth resolution is given by the beamwidth of the antenna, while the Doppler shift is achieved to discriminate between ranges. For conical beams as in Fig. 2.2(b) the spot beam is used to achieve both azimuth and range resolution. In both cases the viewing of the same cell is separated by a time lag (of few minutes) in which the wind is assumed to not change its characteristics.

2.1.3 Other active sensors

Other sensors used to measure ocean parameters include radar altimeters and lidar sensors.

A radar altimeter is a vertically viewing, narrow pulse, pencil beam device that can be used to make a variety of geophysical measurements (see Figure 2.3). Since satellite orbits are determined with submetric accuracies, altimeter measurements can be used to determine several oceanic and geodetic quantities as the sea surface topography, surface elevation and geostrophic currents. The slope of the ocean surface with respect to the geoid along the nadir path can be considered as a measure of the component of the surface current at right angles of the path, and the elevation is a measure of the absolute dynamic topography with respect to the geoid [13]. The determination of geostrophic current information requires, among others, a precise correction for tidal variation pressure and wind stress. Thus, the geostrophic current information from satellites with a high inclination orbit (as Poseidon-2 on Jason-1 and Poseidon-3 on Jason 2) can be averaged over time with the crossing orbits (ascending and descending paths) giving the two components of the surface current vector [9]. From these, the surface geostrophic current field can be determined on a spatial grid with dimensions on the order of a hundred kilometers and average time of several days.

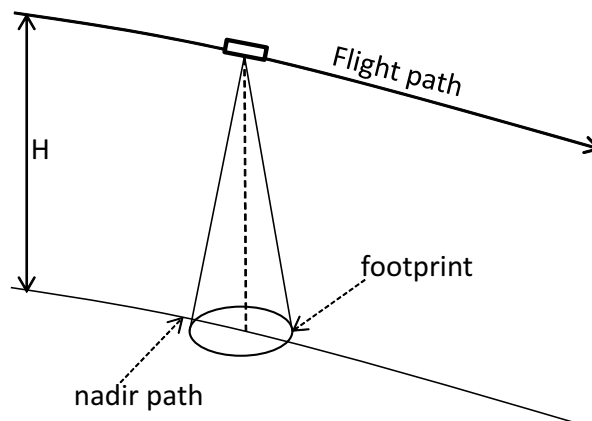


Figure 2.3: Geometry of altimetric measurements of the sea surface.

Lidar sensors measure distances by illuminating a target with a laser and analyzing the reflected light. Satellites-borne lidars have generally been designed to measure aerosols (e.g.

Cloud-Aerosol Lidar and Infrared Pathfinder Satellite Observations, CALIPSO). However, wind speed information may also be derived [32].

2.2 Passive sensors

Passive sensors differ from active sensors in the detection of natural radiation that is emitted or reflected by an object or its surrounding areas. Thus they need an external source of radiation which in most cases is the Sun or the thermal emission of the ocean.

2.2.1 Infrared Radiometer

All bodies radiate electromagnetic energy. Planck's law states that an ideal black-body³ radiates according to [33]

$$B(\lambda, T) = \frac{2hc^2}{\lambda^5} \frac{1}{\exp\left(\frac{hc}{\lambda k_B T}\right) - 1} \quad (2.6)$$

where B [W/(sr·m³)] denotes the spectral radiance, T [K] the temperature, $k_B = 1.38 \times 10^{-23}$ [J/K] the Boltzmann constant, $h = 6.62 \times 10^{-34}$ [J·s] the Planck's constant.

The solar emitted energy has a peak in the visible part of the electromagnetic spectrum, which can pass through the atmosphere. In contrast, the ocean's surface emission peak lies between about 9 μm and 11 μm [8]. This makes the thermal infrared an optimal region for monitoring the radiation of the ocean's surface since the emitted radiance is a maximum there and it varies rapidly with temperature changes.

An infrared (IR) radiometric sensor records the detected radiance in specific wavebands λ_n . The individual measurements in each channel, n can be expressed as an equivalent black-body brightness temperature of the surface, B_s [10]. The brightness temperature is obtained as a function of the surface temperature, T_s , the emissivity of the water, ϵ_s , and the temperature of the atmospheric emission T_a [10, 34]. The radiance intercepted by a particular spectral channel is obtained with the integration of eq. (2.6) with respect to the wavelength over the measured waveband and convolved with the spectral sensitivity of the sensor.

The atmosphere allows the infrared radiation to pass through it in two "windows". These are found between 3.5 μm and 4.1 μm and between 10.0 μm and 12.5 μm . The latter is often used for two separate wavebands, generally referred as the "split window channels".

Data from thermal channels of IR sensors flown on polar-orbiting and geostationary meteorological satellites have been used for the determination of sea surface temperature at depth less than 0.1 mm [9, 35] and to estimate surface current velocities as studied in Chapter 5.

³A black body is an idealized body that absorbs all incident electromagnetic radiation, regardless of frequency or angle of incidence, and, in thermal equilibrium (constant temperature), emits electromagnetic radiation according to Planck's law.

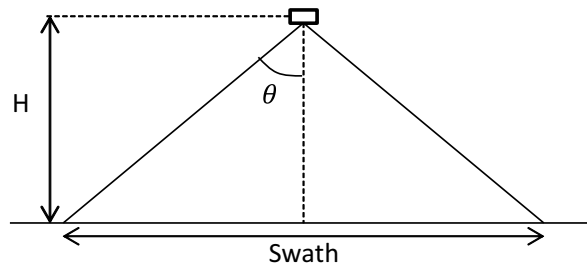


Figure 2.4: General geometry of the AVHRR sensor.

Currently used IR sensors to measure the ocean surface include the Advanced Very High Resolution Radiometer version 3 (AVHRR/3) sensors on board the National Oceanic and Atmospheric Administration (NOAA) family of polar orbiting platforms (POES) and MetOp-A/B satellites as well as the MODerate-resolution Imaging Spectrometer (MODIS) on-board the Terra and Aqua satellites. Figure 2.4 shows the general geometry for AVHRR sensors. With a nominal height of $H = 833$ km the footprint at nadir is 1.1 km, and with a cross-track scan $\theta = \pm 55.4^\circ$ the swath width is about 2500 km [8]. AVHRR data have been used for the evaluation of the algorithm for surface currents retrieval explained in Chapter 5, which has been used in Paper D.

2.2.2 Other passive sensors

Microwave radiometers and color scanner radiometer sensors have also been used to measure oceanic parameters.

Typical applications of microwave radiometry concerning oceans are: sea salinity, sea surface temperature, wind speed and direction, sea ice detection and classification. However, in an attempt to measure properties of the sea from space, the intervening atmosphere will disturb the process when operating at high microwave frequencies (e.g. >10 GHz), and corrections might be required. Also, at some frequencies and for some applications the Faraday rotation in the Ionosphere must be taken into account [9, 36].

The most significant product of color scanner radiometers include the collection of so-called ocean color imagery. The “color” of the ocean comes from substances in the water, particularly phytoplankton (microscopic, free-floating photosynthetic organisms), as well as inorganic particulates [8, 10].

Surface wind retrieval from synthetic aperture radar

In Chapter 1 surface winds were introduced as an essential parameter for the study of the ocean. In Chapter 2 several satellite sensors were described which produce information about ocean surface winds. From these, SAR sensors are the ones who achieve finer resolution independently of the weather conditions.

The relationship between SAR measurements and surface winds, as in the case of scatterometers, is determined by changes in σ_0 of the ocean surface. The availability of C-band SAR data from satellites for civilian applications (e.g. ERS-1/2, Radarsat-1/2 and Envisat), and the direct interaction of the C-band wavelengths (5-6 cm) with the ocean surface (see Section 3.1) has made C-band the favorite frequency for SAR wind estimation [37–51]. However, some work has also been done on wind retrieval with L-band and X-band SAR data [52, 53].

Although previous work has studied C-band SAR surface winds, Paper A contributes with the retrieval at different resolutions, being validated for offshore areas, with an explicit assessment for both wind direction and wind speed with respect to modeled and scatterometer data. Moreover, the algorithm developed in Paper A aims for an operational retrieval in mid-tropical latitudes worldwide.

The SAR wind retrieval of Papers A and B used both wind direction and wind speed information derived from the SAR image, which are related to the studies performed in [37–42, 45, 46]. However, the retrieval in the polar latitudes of Paper B was limited by the conditions in the marine atmospheric boundary layer. Thus, the work in Paper C used modeled surface wind directions, as in [43, 48, 50], for the determination of SAR wind speeds.

This Chapter summarizes the background and methodology behind the determination of surface winds with SAR data used in Papers A, B and C, divided in the following manner: Section 3.1 describes the relationship between the backscatter of the ocean with SAR measurements; Section 3.2 explains the wind speed retrieval from geophysical model functions; Section 3.3

explains the relationship between surface wind directions and streak features in SAR imagery; and Sections 3.4 and 3.5 refer to the general procedure and data used for the wind derivation, evaluation and assessment of Papers A, B and C.

3.1 Backscatter properties of the ocean surface

The σ_0 (see eq. (2.2)) of the ocean surface is measured by the average intensity of the SAR return signal. In general, radar return is related to sea surface roughness. This roughness, in turn, is usually indicative of and driven by the local wind. The changes in backscattered power as a function of wind speed and direction form the basis of the remote sensing of wind speed and direction from spaceborne radar [54].

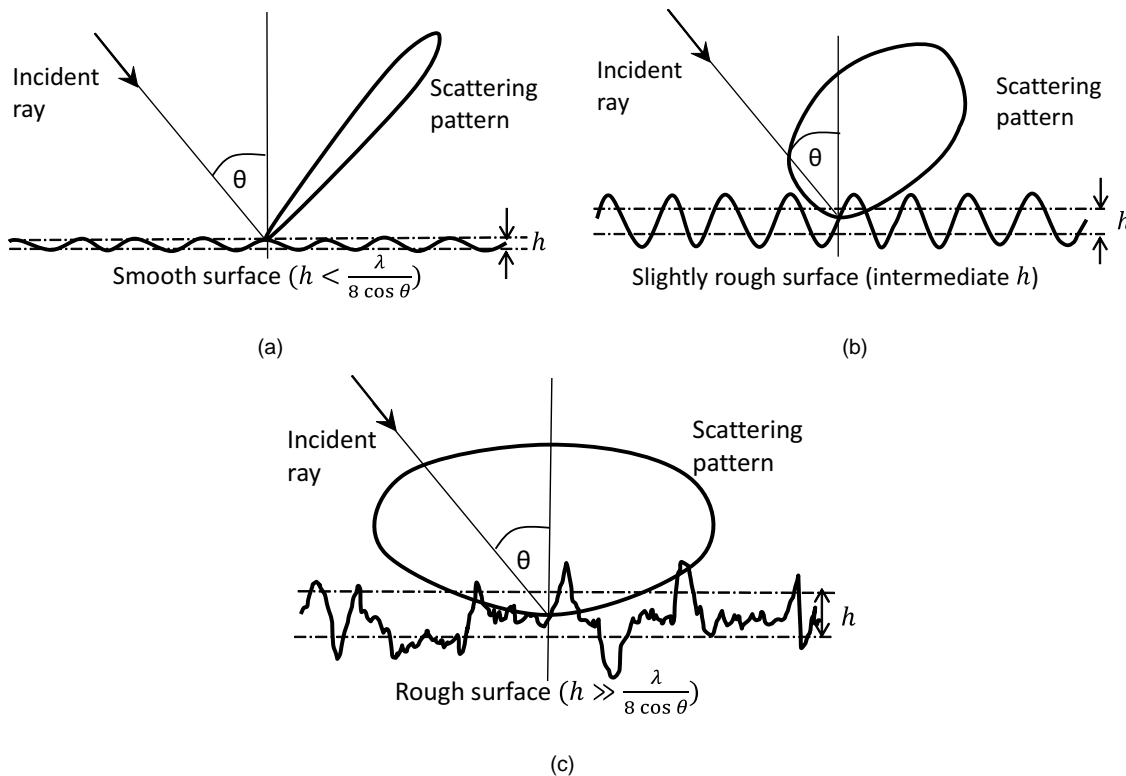


Figure 3.1: Schematic representation of microwave scattering of the ocean surface.

At very low wind speeds and at microwave frequencies, the ocean surface is smooth. Under these conditions, the electromagnetic (EM) wave from a side looking radar will reflect at an angle equal and opposite to the incidence angle and yield little or no backscattered power (see Fig. 3.1(a)). The Rayleigh criterion defines a surface as smooth if [14]

$$h < \frac{\lambda}{8 \cos \theta} \quad (3.1)$$

where h is the surface roughness, defined as the root-mean-square (rms) height relative to a perfectly smooth surface, λ is the wavelength of the wave and θ is the angle of incidence. Using

the Rayleigh criterion, for instance, with a SAR operating at $f_c = 5$ GHz with an incidence angle of 50° , an ocean roughness with $h < 11$ mm will have most of its energy in the specular component.

As the wind speed increases, the surface roughness and backscatter power increases (see Figs. 3.1(b)-3.1(c)). Thus, for an obliquely viewing instrument the amount of backscatter increases as the roughness increases.

For a homogeneous medium with a slightly rough surface (eq. (3.1)), the scattering can be described using the Bragg model [14]. The Bragg model is therefore useful for describing the backscatter from the ocean surface. The periodic structure of ocean waves modulates the radar waves [55]. This modulation is often referred as resonance of the radar waves. In first order Bragg theory the resonant water wave length Λ is related to electromagnetic wavelength λ by

$$\Lambda = \frac{\lambda}{2 \sin \theta} \quad (3.2)$$

In the range of microwaves of about 1 to 18 GHz a radar is sensitive to small perturbations (ripples) on the ocean surface [8, 56]. The Bragg wavelengths vary from approximately 1-20 cm, a range which includes capillary and short gravity waves.

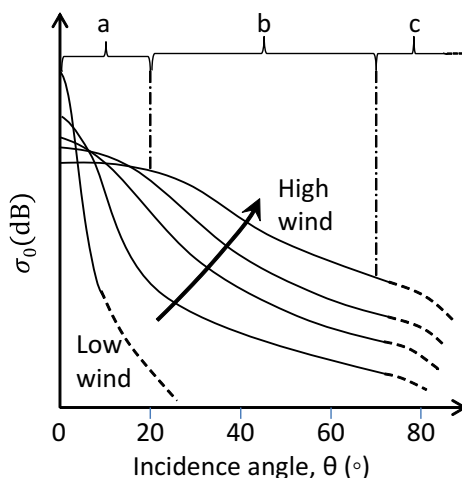


Figure 3.2: Sketch of variation of σ_0 with the incidence angle and wind speed.

Figure 3.2 illustrates the variation of σ_0 with the incidence angle θ , under different wind conditions [8, 14, 57]. At low incidence angles, the (a) region, specular reflection is the dominant process. For a very calm sea there is a narrow angular response giving high return at 0° which rapidly drops off as the incidence angle increases. For a somewhat rougher surface under moderate winds the response is weaker, but does not decay as rapidly with the increasing incidence angle. At high winds σ_0 is even lower, but with very little drop-off with the incidence angle. At incidence angles between about 20° and 70° , the (b) region, the behaviour of σ_0 is quite simply described. At a given θ it increases with the sea state, while there is an approximately linear reduction of σ_0 in dB with the incidence angle. Finally, at high incidence angles,

the (c) region, the value of σ_0 appears to drop off more rapidly with θ , reaching very low values when approaching to 90° .

Because the dependence on wind speed is so different between zero-to low and moderate-to-high incidence angles it is important to treat them separately when seeking useful algorithms to relate the wind behaviour and σ_0 . In general, the first (a) region is used to estimate wind speed by altimeter sensors, while the second (b) region has been exploited by side looking sensors as scatterometer and SAR. Modeling approaches of σ_0 should also consider the effects of frequency, polarization and the wind direction.

3.2 Wind speed from geophysical model functions

The nearly linear variation of σ_0 with the wind speed at moderate-to-high incidence angles for a given frequency, polarization and wind direction has been empirically established in the derivation of Geophysical Model Functions (GMFs). These relationships are generally defined for vertically polarized (VV) EM waves in the following way

$$\sigma_0^{VV} = A(\theta, U_{10}) [1 + B(\theta, U_{10}) \cos \phi + C(\theta, U_{10}) \cos 2\phi]^\gamma \quad (3.3)$$

where U_{10} is the neutral wind speed at the height 10 m, θ is the local incidence angle, and ϕ is the wind direction with respect to the radar look direction. A , B , C , are functions of U_{10} and θ , incorporating the upwind-downwind and upwind-crosswind effects. The power γ effectively generates high order Fourier terms in the definition of σ_0 .

The wind direction, ψ is normally expressed as the direction from where the wind comes from with respect to the North (meteorological convention) [58]. However, a correct parametrization of σ_0 requires the wind direction expressed in terms of the antenna look direction χ as ϕ by using (see Fig. 3.3)

$$\phi = \psi - \chi \quad (3.4)$$

Widely used GMFs for C-band SAR data include CMOD4 [59], CMOD-IFR2 [60], CMOD5 [61], and CMOD5.N [62]. Figure 3.4 illustrates CMOD-IFR2 and CMOD5.N for an incidence angle of $\theta = 35^\circ$. The backscatter power is greatest when the radar look direction and the wind direction are aligned. However, there is a slight asymmetry. The backscattered power for winds blowing directly toward the radar is greater than the power for winds blowing directly away from the radar.

The asymmetry in the GMFs is normally used by scatterometer sensors in order to determine the wind speed and direction through measurements of σ_0 at different look directions (e.g. 2 with Seasat, 3 with ERS1-2 and MetOp-A, see Section 2.1.2). However, the fact that SAR measures the ocean backscatter with only one look direction it follows an indetermination of eq. (3.3). Thus, it is necessary to obtain a priori information in either wind direction or wind speed in order to invert the GMFs as eq. (3.3).

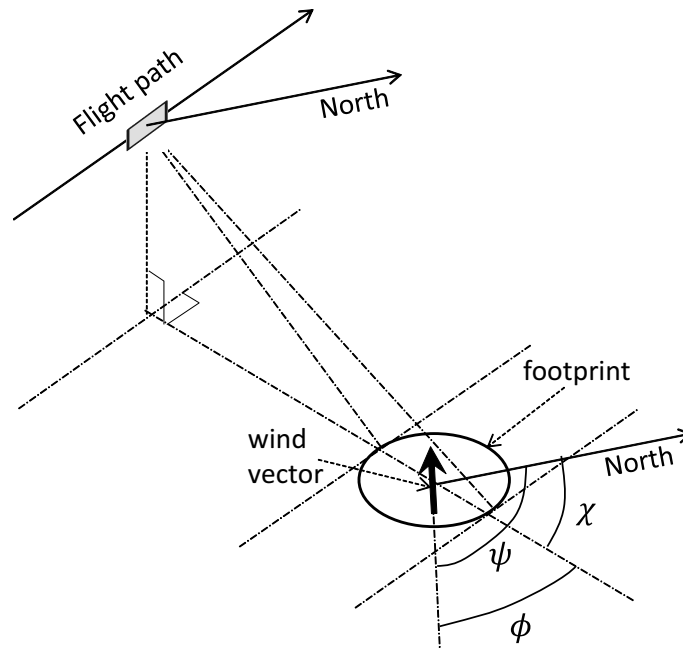


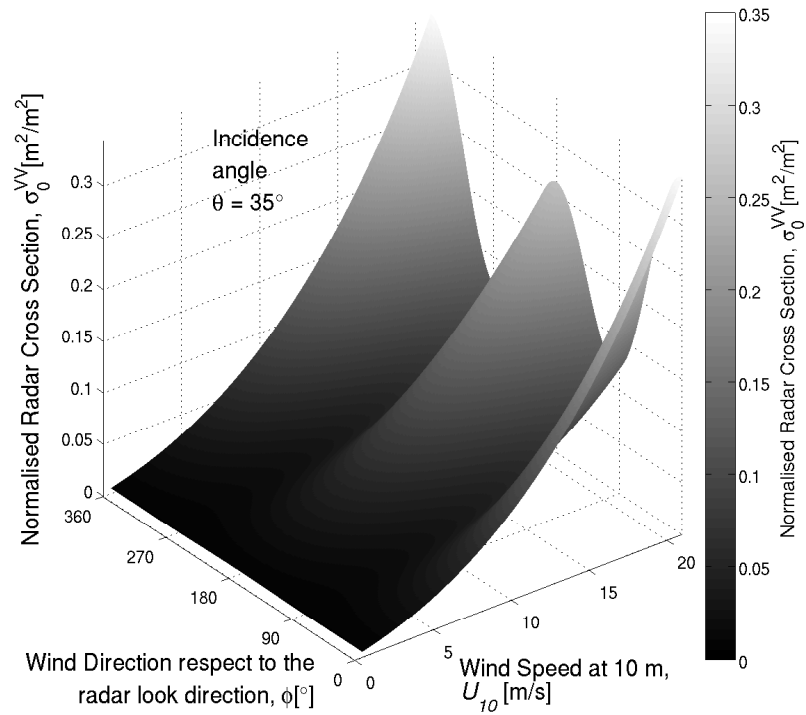
Figure 3.3: Geometry for the determination of the wind direction. For a sidelooking SAR geometry the wind direction with respect to the north (meteorological convention) is represented by ψ , while with respect to the radar look direction it is represented by ϕ . The radar look direction with respect to the north is given by χ .

The retrieval of U_{10} can be accomplished in the following manner. Selecting a GMF, a lookup table of σ_0^{VV} may be produced for each subimage for θ , and ϕ . Then, a value of σ_0^{VV} is obtained for the considered wind cell. Finally, U_{10} is inverted by applying a linear curve fitting around σ_0^{VV} from the available points of the corresponding lookup table.

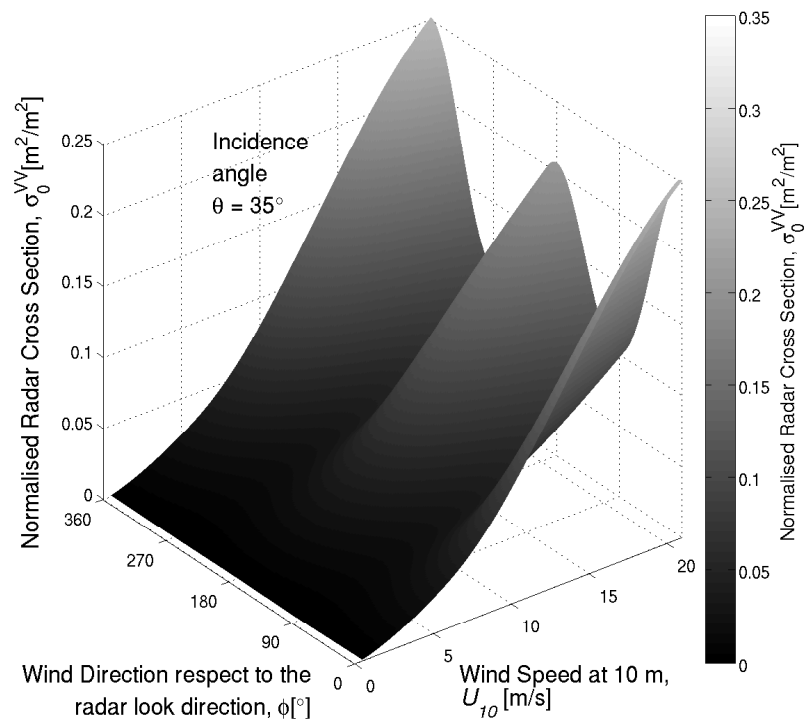
The nominal accuracy on wind speed retrievals is ± 2 m/s and GMFs functions are valid for wind speeds between 2 and 28 – 50 m/s, and incidence angles of $20^\circ - 60^\circ$ [59–62]. GMFs apply to open oceans with a near-neutral atmospheric stability.

In a simplified way, the near-neutral stability condition is given when the air in the atmosphere keeps a constant heat. This is represented as an equilibrium due to the balance between a driving scale pressure gradient force¹, the Coriolis force due to the rotation of the Earth, and the dissipating frictional force [63]. In this case the wind profile is defined as a logarithmic

¹The pressure gradient force is produced when there is a difference in pressure across a surface. This difference then implies a difference in force, which can result in an acceleration according to Newton's second law, if there is no additional force to balance it. The resulting force is always directed from the region of higher-pressure to the region of lower-pressure.



(a) CMOD-IFR2



(b) CMOD5.N

Figure 3.4: The CMOD-IFR2 and CMOD5.N geophysical model functions for an incident angle $\theta = 35^\circ$. The values of σ_0^{VV} , are modeled as a function of the wind speed, U_{10} [m/s], and the wind direction with respect to the radar look direction (ϕ [$^\circ$]).

function of the height z^2

$$U(z) = \frac{u_*}{\kappa} \ln \left(\frac{z}{z_0} \right) \quad (3.5)$$

where u_* is the friction velocity³, the von Kármán's constant is $\kappa = 0.4$, and z_0 is the roughness length⁴.

However, the radiation balance of the surface and thermal inertia of the water leads to temperature differences between the surface and the air. These temperature differences lead to the formation of an either stable or unstable boundary layer. In a stable boundary layer the atmosphere is cooled from below, which normally occurs at night [63] and in the Polar regions [66]. In contrast, in a unstable boundary layer the heat input from below dominates. Here marine boundary layer rolls and cellular convection patterns can develop [67]. Thus, the stability has a large impact on turbulence structure and the vertical variation of wind and temperature [68].

3.3 Wind direction from SAR image streaks

The friction at the surface and the transport of sensible and latent heat⁵ across the ocean surface defines the lower part of the atmosphere as the marine atmospheric boundary layer (MABL) [70, 71]. Here there are frequent horizontal layers distinguished by differences in speed or direction or both [63, 67, 72]. Such layers may form when fluid masses with different environmental histories meet; or a single layer may stratify when, for example, the air at the Earth's surface becomes heated and moistened. Any sharp variation in humidity, temperature, or density is generally accompanied by a change in flow velocity. The Coriolis force may turn the flow when it is in balance with a horizontal density gradient or with the viscous force, as occurs next to a solid boundary (e.g. the ocean's surface and air interface), where Ekman layers are developed (see Section 4.1.1).

When one layer of a certain velocity is adjacent to a flow of a different velocity, the flow at the interface changes with height, sometimes very sharply, leading to local vorticity extremes associated with an inflection point in the mean velocity profile. The inability of the fluid to sup-

²The logarithmic wind profile for a neutral atmospheric boundary layer is usually applicable for heights below the Prandtl height z_p . A scale analysis allows to define z_p as a function of the friction velocity u_* and the coriolis parameter f with $z_p \approx 0.01 u_*/f$. Putting in numbers ($u_* = 0.5$ m/s, $f = 0.0001$ s⁻¹) gives a typical height $z_p = 50$ m [63, 64].

³The friction velocity represents a reference wind velocity defined by the relation $u_* = \sqrt{\tau/\rho}$, where τ is the Reynolds stress and ρ is the density [65].

⁴Roughness length (z_0) is a parameter of the vertical wind profile equations that model the horizontal mean wind speed near the ground; in the logarithmic wind profile, it is equivalent to the height at which the wind speed theoretically becomes zero [63].

⁵The transport of sensible and latent heat fluxes to the atmosphere act as a second positive feedback mechanism effective in the thermal interaction processes through heat flux exchange. As a result, the atmosphere obtains energy from the ocean, which intensifies atmospheric motions. [69].

port these local extremes in vorticity produces the physical mechanism leading to readjustment in the flow pattern. If the frictional forces are not strong enough to support the local strains in the fluid, the flow becomes unstable of all perturbations [67, 73]. Here the water and air interact until they change the basic flow into a more stable pattern, an alteration that may involve equilibrium secondary flows or local patches of turbulence [63, 67]. This turbulence modifies the wind profile of eq. (3.5) as

$$U(z) = \frac{u_*}{\kappa} \left[\ln \left(\frac{z}{z_0} \right) - \Psi \left(\frac{z}{L_*} \right) \right] \quad (3.6)$$

where L_* is the Obukhov length, and Ψ represents a correction function of the logarithmic wind profile.

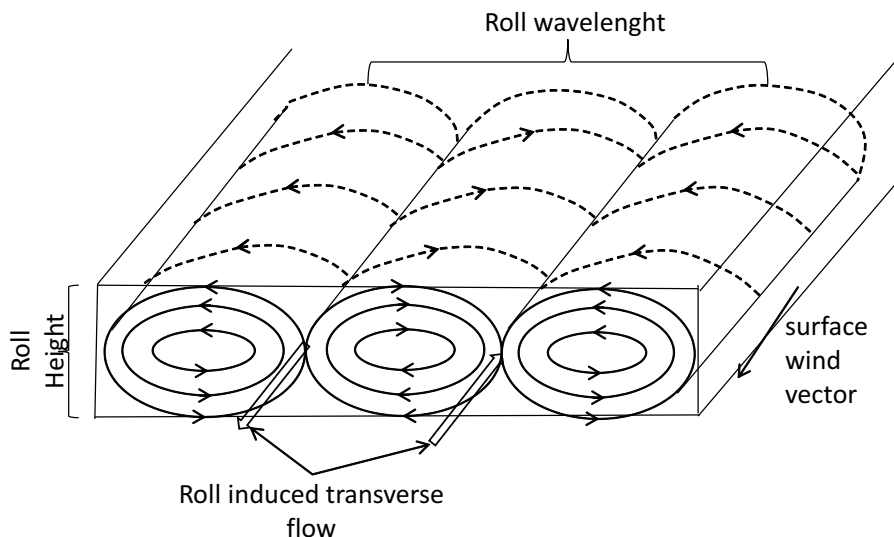


Figure 3.5: Schematic of idealized roll vortices above the sea surface.

In a seminal paper, *Gerling* [74] observed linear features following the direction of the wind on the scale of a few kilometers in Seasat imagery. These features have been more recently associated, in most of the cases, to the signature of roll vortices [70, 71, 75, 76]. Figure 3.5 shows a schematic view of an idealized field of roll vortices. The axes of the boundary layer rolls are oriented nearly parallel to the mean boundary layer wind shear vector. The ascending and descending regions of circulation lead to a decreased and increased sea surface roughness, which results in lines of enhanced (downward flow) and decreased (upward flow) backscatter [54, 71, 74, 76–78]. Moreover, other processes (e.g. Langmuir cells, surfactant streaks, wind shadowing) have also been reported to produce streaks in a SAR image nearly aligned with the wind direction [79, 80]. These processes are usually associated to variations in surface wind speed and roughness produced by the vertical transport of momentum in the MABL.

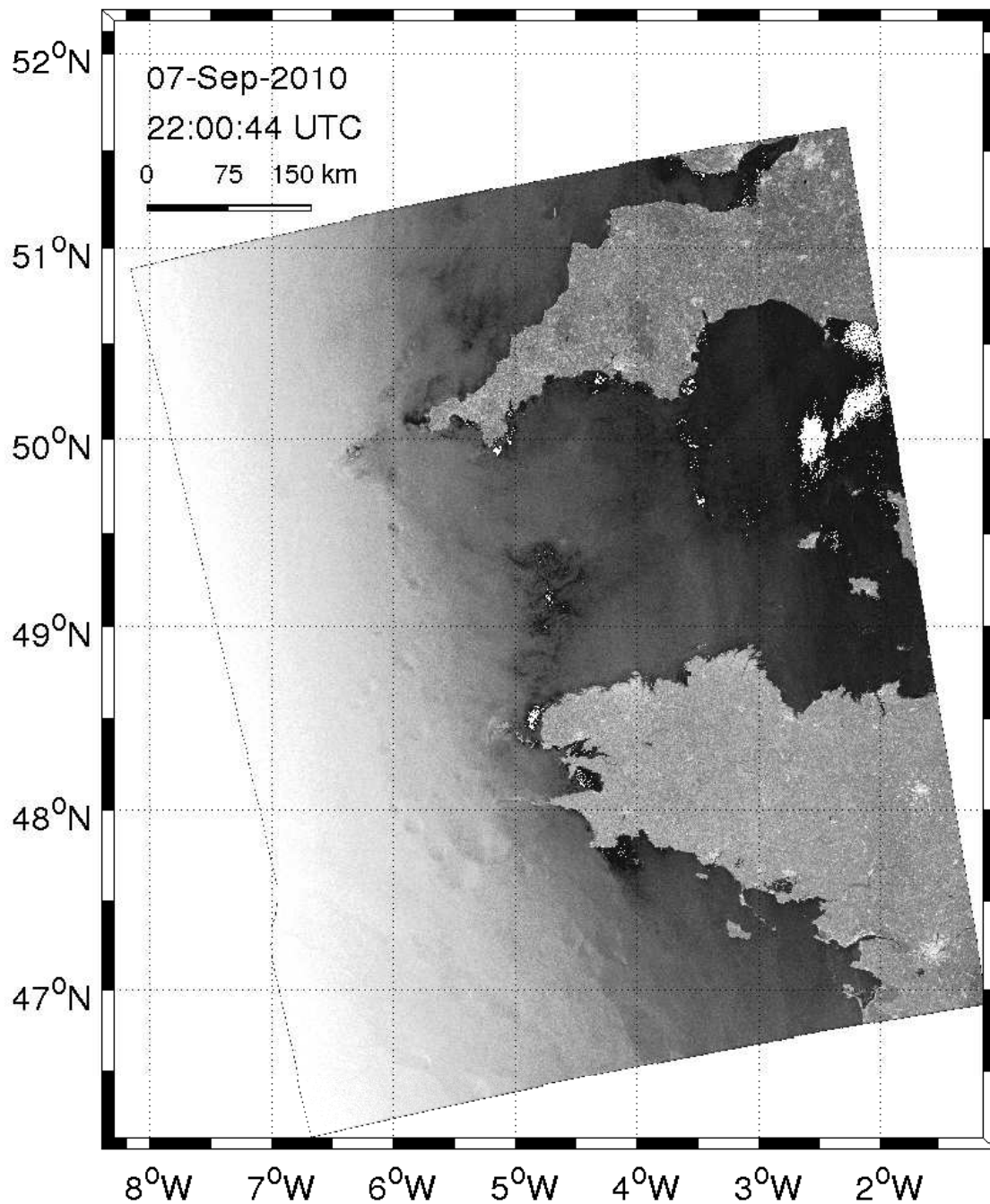


Figure 3.6: Example of a SAR image acquired by ASAR sensor onboard Envisat. The data was acquired in the West of the English Channel (asc., VV pol).

Numerous studies have analyzed rolls in the MABL. In [81] a method was developed for determining roll characteristics in radar data and related wavelength and aspect ratio (width/height) of observed rolls to convective instability and MABL depth. In [73] it was shown that the parameter z/L_* is useful to determine the duration of the rolls. The analysis with weather

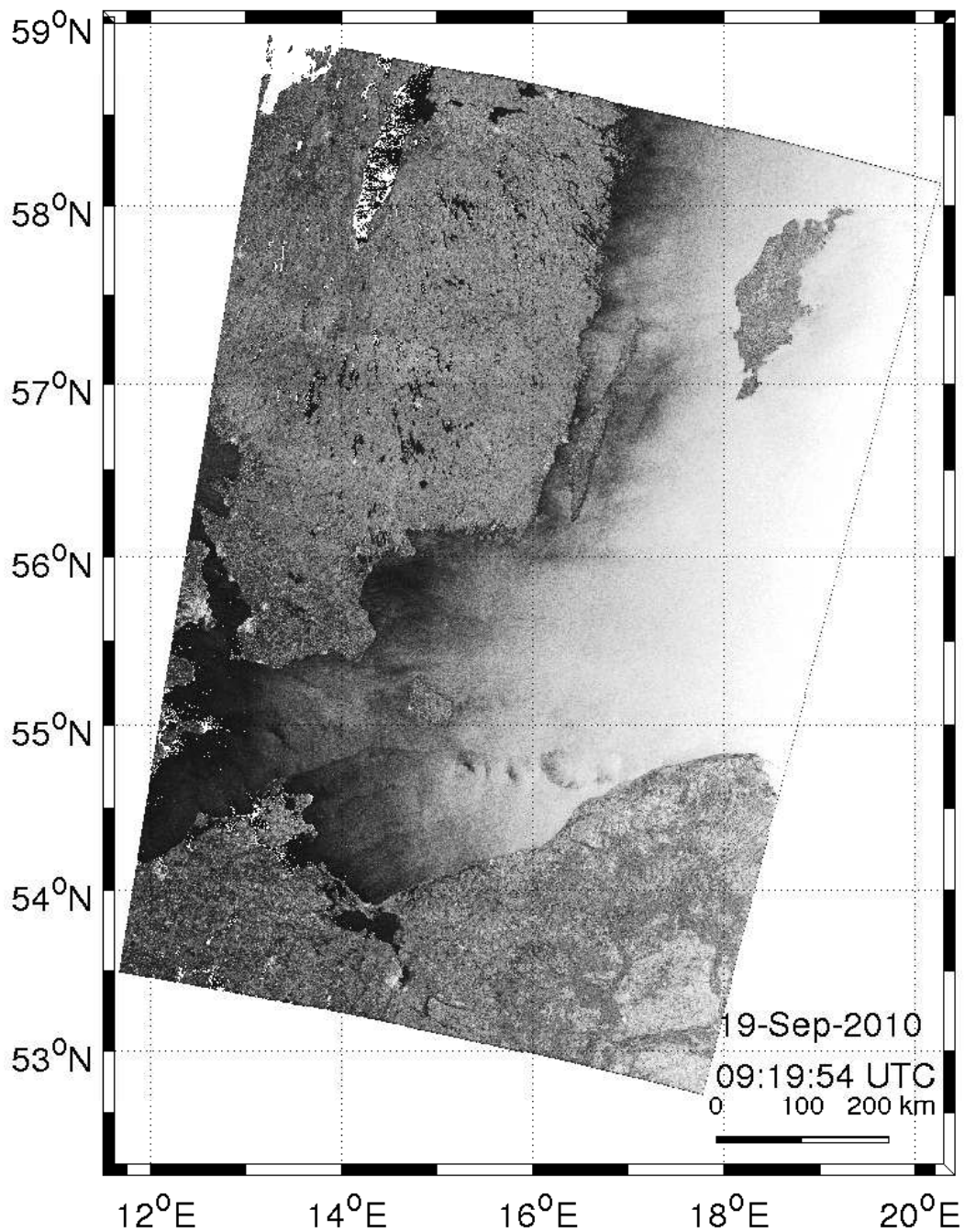


Figure 3.7: As 3.6. The data was acquired at the Baltic Sea (desc., VV pol.).

surveillance radar in [71] identified rolls in 35% to 69% of the radar volumes of four hurricane rainfalls. These rolls had typical wavelengths of 1450 m, aspect ratios of 2.4 and with an induced transverse flow of ≈ 7 m/s (see Fig. 3.5). The rolls were nearly aligned with the surface wind vector. The mean wind direction minus the roll direction varied from approximately -30° to 10° with a mean of -4° and a most probable orientation of -10° . Negative angles imply

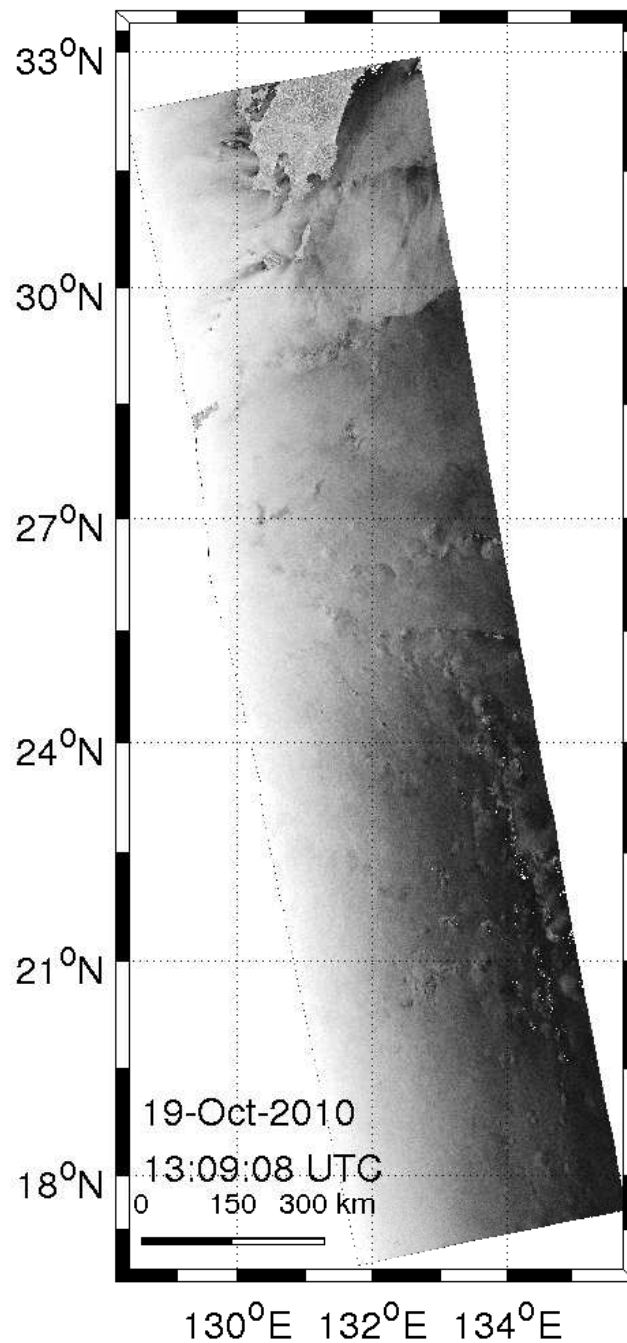


Figure 3.8: As 3.6. The data was acquired at the Southwest of Japan (asc. VV pol.).

that the downwind axis of the rolls is oriented towards the storm center. In [78] it is concluded that the MABL is ideally suited for roll formation because of an instability associated with an inflection point that is characteristically present in the radial component of the wind profiles. The results from the comparison between aircraft and SAR measurements in [76] verified typical roll wavelengths of 900 m and a height of 500 m, giving an aspect ratio of about 1.8. Thus

it can be concluded that rolls consistently occur in moderate winds (greater than 5 m/s) and slightly unstable stratification [67]. When convection is a dominant mechanism, the angle of the rolls is nearly 0° . The characteristic scale length is 1 to 4-km separation between bands with lengths in the hundred of kilometers [67, 71]. Nevertheless, the probability of roll occurrence can vary between 10% and 80% depending of the geographical location and seasonal conditions [82].

Figures 3.6-3.8 show different images acquired by the Advanced SAR (ASAR) sensor on-board the Envisat Satellite in different locations worldwide during September-October 2010. The backscatter variations in the English Channel area in Fig. 3.6 suggest a wind pattern oriented along the coastline, with signatures of rain cells in the middle of the image (6°W - 5°W) [83]. The Baltic Sea area in Fig. 3.7 indicates a wind pattern close to the West-East direction. Finally, the area at Southwest of Japan in Fig. 3.8 presents a more complex pattern of several wind fronts at the Northern part of the image and rain cells at the southern part of the image. The extraction of the wind direction from the analysis of these images is discussed in Section 3.4.

3.4 Computation of surface winds

Section 3.1 showed that the backscatter of the ocean surface detected by SAR sensors is related to the wind speed, wind direction, polarization of the EM wave, and the acquisition geometry through GMFs (see eq. (3.3)). The fact that SAR sensors have only one look direction implies only one equation to solve the unknown wind direction and speed. Thus, a common approach is to obtain one of them in an independent way to invert the other parameter from a GMF.

It is common to have as the independent parameter wind directions from a weather prediction model (WPM) [48, 84–87], or another retrieval from the SAR image itself [37, 44, 46, 51, 88–92]. Wind directions from a WPM have the advantage of being regularly available and have a good accuracy from validations with in-situ reference data. However, since they are generally provided in scales of about 0.5° of latitude and longitude for global estimations (which approximates 50 km grid spacing in latitude), the small scale variations in the wind direction are averaged out.

The retrieval of both wind direction and speed from SAR images depends of the availability of the additional information not considered by the GMFs. This extra information can be related to wind streaks in the SAR image due to a convective behaviour in the MABL [74, 77], as mentioned in Section 3.3, or more recently, to the relationship between wind speed and polarization for fully polarimetric SAR measurements [51]. The association between the SAR image streaks and the wind direction has the advantage that it does not require fully polarimetric SAR data. The horizontally co-polarized SAR data (HH polarization) with σ_0^{HH} can be also used to invert wind speeds from eq. (3.3) with the addition of a polarization ratio depending of the incidence

angle, θ [14, 49, 93–95].

The work of Papers A and B in this thesis has considered wind directions obtained from the analysis of streak features in the SAR data as described in Section 3.3. In Paper C, however, the wind directions were obtained from a WPM. In Papers A and B the SAR wind speed inversion used wind directions retrieved from the intensity gradients in the SAR image. The validation results in Paper A showed that wind direction retrievals performed well in offshore areas, with mean and standard deviations with respect to in-situ data of 9° and 25° for 5 km wind resolution cells.

The MABL is often stable in polar marine surfaces [66]. This is because stable thermal stratifications are usually found over waters that are colder than the air above [63, 64]. Thus, the streaky features in the SAR imagery, derived from convection and thermal instability, used to extract wind directions are not always available in polar areas [42, 82]. In Paper B it was necessary to compute daily average values of wind velocity over the Amundsen Sea area (130°W - 100°W and 73°S - 68°S). However, the restriction of available SAR data to an average of 3 images per day together with the limited availability of streak features to determine the wind direction made it necessary to use a time window of 2 days, with up to 6 SAR images, to estimate the daily average values of the wind field. Therefore, in Paper C, it was decided to use wind directions from a WPM to compute SAR wind speeds.

Figure 3.9 shows wind directions for segments of the ASAR images of Figs. 3.6-3.8. The wind directions from the SAR analysis are represented in different colors (red, yellow) according to their resolution, while wind directions from a model are in magenta. Although they visually present a generally good agreement, the SAR wind retrievals includes much more details in the wind direction variations due to their higher resolution. This variation in the agreement as a function of the resolution is studied in Paper A.

3.5 Reference data

Surface wind estimates from other sources are necessary either to assess the validity of the SAR wind vector retrievals as in Paper A and Paper B, or as an external data source of wind directions for SAR wind speed retrievals as in Paper C. Nevertheless, differences in acquisition time, location and resolution should be taken into account.

3.5.1 In-situ sensors

The in-situ reference surface wind data used in this thesis was obtained from three different sources: the U.K. Met Office through the project MyOcean; the Swedish Meteorological and Hydrological Institute (SMHI); and the Korea Polar Research Institute (KOPRI). The data from the U.K. Met Office correspond to two different locations along the English Channel (see Fig. 7

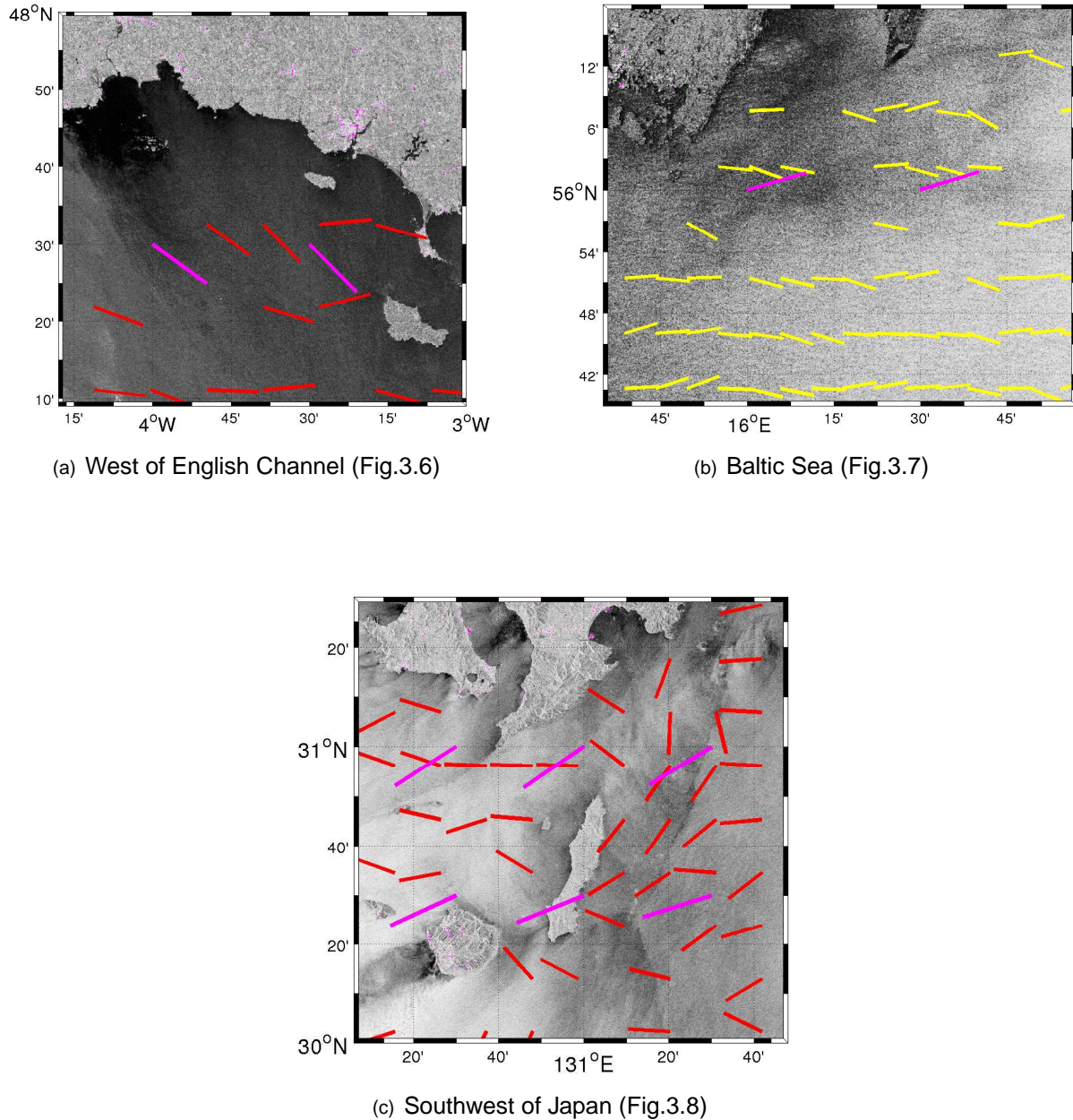


Figure 3.9: Segments of SAR images from Figs. 3.6-3.8 with wind directions from the streak pattern determination of Sec. 3.3 (red \rightarrow 20 km, yellow \rightarrow 10 km) and with wind directions from a weather prediction model (magenta \approx 50 km).

of Paper A). From SMHI there were three different locations considered in the coastal areas of Sweden with a surrounding land coverage lower than 0.4% in 100 km² (see Fig. 8 of Paper A). From KOPRI the measurements were located at the Lindsey Island [96], in the surroundings of the Amundsen Sea.

To compare with the SAR wind retrievals, the in-situ measurements were adjusted in time and converted into 10 m neutral winds U_{10} . Since the measurements were normally available

in intervals of 1 h they were linearly fitted to the time of the SAR data acquisition. Afterwards, they were adjusted into 10 m neutral winds using the relationships in eqs. (3.5) and [97]

$$z_0 = \alpha \frac{u_*^2}{g} + \beta \frac{\mu}{u_*} \quad (3.7)$$

where z_0 is the roughness length, u_* is the friction velocity, α is the Charnock constant, whose value is between 0.018 and 0.030 [98], $\beta = 0.11$ is the limiting roughness for an aerodynamically smooth flow, $g = 9.81$ m/s² is the acceleration of gravity, and μ is the air viscosity computed as a function of the air temperature T_a [°C] with [99]

$$\mu = 1.326 \cdot 10^{-5} \cdot (1 + 6.542 \cdot 10^{-3}T_a + 8.301 \cdot 10^{-6}T_a^2 - 4.84 \cdot 10^{-9}T_a^3) \quad (3.8)$$

With an initial $u_*^0 = 0.036 \cdot U$, z_0 and u_*^n were estimated in an iterative way from eqs. (3.5) and (3.7) (with the height z of the sensor) until a convergence was found as $|u_*^n - u_*^0| < tol = 0.00001$. Thus, U_{10} was computed from the solution of z_0 and u_*^n and a height $z = 10$ m in eq. (3.5).

3.5.2 ASCAT scatterometer

In this thesis wind data from the Advanced SCATterometer (ASCAT) onboard the MetOp-A satellite at 25 km resolution has been used. The ASCAT wind products are distributed through a ftp server with a delay of approximately 30 minutes from sensing time and as a Global Ocean and Sea Ice Facility (OSI SAF) product with a delay of approximately 2.5-3 hours from sensing time [100]. The wind product validation has a rms error of 1.3 m/s in the wind speed and 16° in wind direction when compared with the European Centre for Medium-range Weather Forecast (ECMWF) winds and a rms wind component error of approximately 1.8 m/s against buoy winds [101].

ASCAT covers nearly 70% of the ice-free oceans every day. Each file represents a complete satellite orbit, beginning with the ascending node at the equator, and ending at the next ascending node near the equator. Fig. 3.10 shows data acquired by the ASCAT sensor on June solstice 2010. Thus, the wind measurements stop at about 60°S because of ice coverage.

Due to the characteristics of the ASCAT and ASAR sensor coverage, the comparison of their retrievals done in Paper A had to allow a time delay between the datasets of up to 2 h from the ASAR observation time. Also, for a direct comparison taking into account the variation of the retrievals with the resolution, the ASCAT data was spatially interpolated into the locations of the ASAR wind vectors.

3.5.3 Weather prediction models

In Section 3.4 it was mentioned that data from WPM were used for either comparison with the SAR retrievals or as an input for wind direction information. Thus, two WPM were used

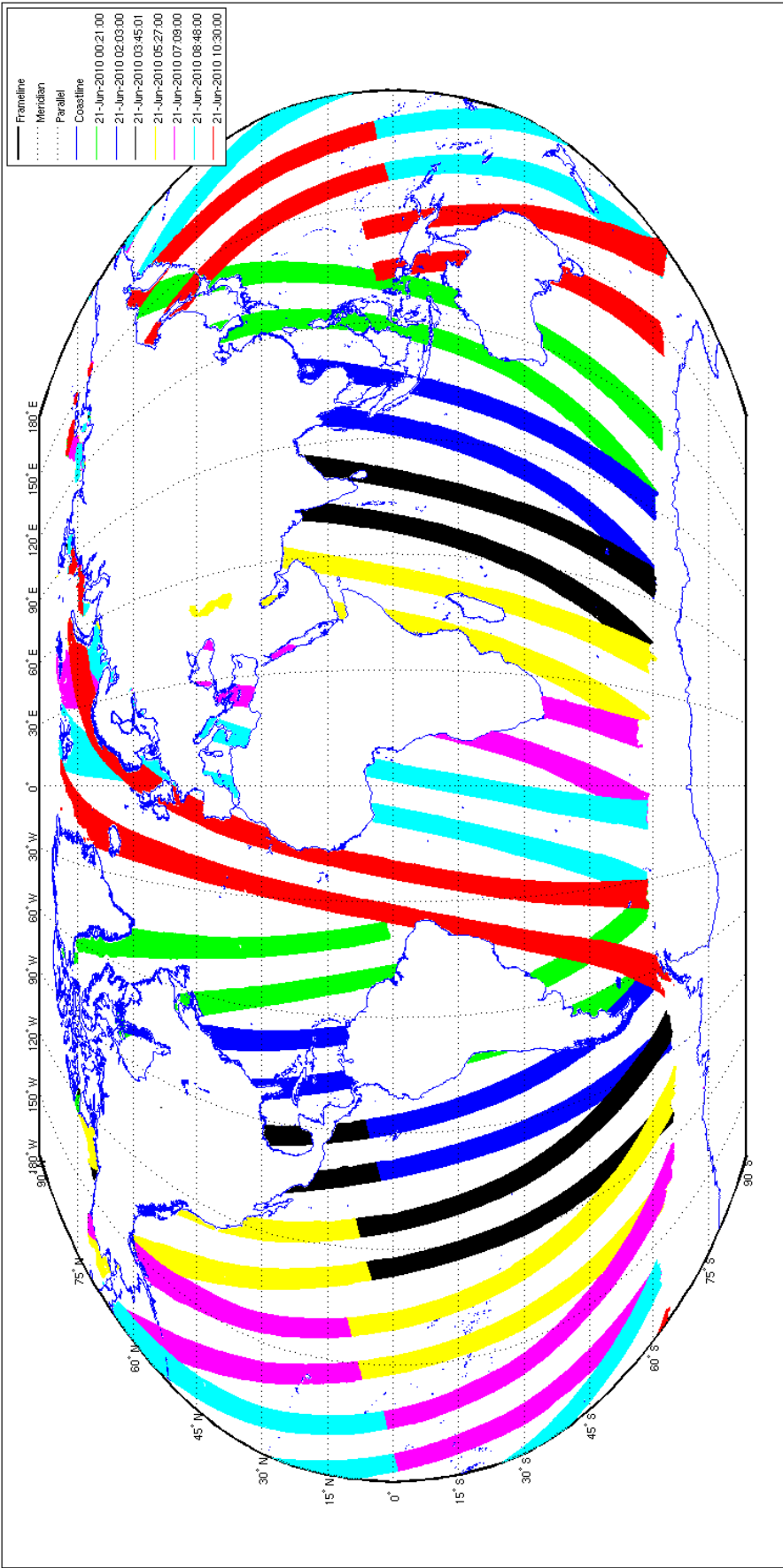


Figure 3.10: Several of the ASCAT orbits for the June solstice of 2010. For clarity, only seven orbits were represented, each one with a particular color. The time indicated in the legend corresponds to the starting time of the orbit.

as a source of 10 m neutral wind data. The Global Forecast System (GFS) model, from the National Center of Environmental Prediction (NCEP) of the National Oceanic and Atmospheric Administration (NOAA) [102], was used in Paper A. The ERA-interim reanalysis products, from the European Center of Medium Range Weather Forecast (ECMWF) [103], were used in Papers B and C. Both the GFS and ERA-interim are global spectral data used for and forecast model systems. The data sets are produced every six hours at 00, 06, 12 and 18 UTC. In every run these models provide 10 m neutral wind vectors and global coverage at a resolution of 0.5° in latitude and longitude [102, 103].

GFS model data were used in Paper A, due to its near-real-time availability, with forecast at intervals of 3 hours. This choice aims for an operational use of the SAR algorithm with the resolution of the 180° ambiguity using the GFS wind direction estimates.

ERA-interim reanalysis data were used in Papers B and C, since so far these data have been considered the most accurate meteorological reanalysis product covering the Amundsen Sea area [104].

The Papers A, B and C include the fitting of the WPM to the ASAR data. Firstly, the two wind predictions closest in time were averaged to the ASAR acquisition time. Secondly, the model estimates were interpolated to the exact locations of the ASAR wind resolution cells.

An application of surface winds for oceanography in Antarctica

The Earth's surface around the Arctic and Antarctic is largely covered by water and ice. The ice and sea-ice cover changes the planetary albedo and can thus affect the steady-state global-mean temperature [3, 105]. Sea ice also acts as a thermal blanket, insulating the ocean from the above atmosphere. Since the oceans are warmed from above, and heating makes water less dense, it could be expected that greater depths are isolated and stagnant since light surface water would be resistant to mixing downwards and would sit like a lid on the ocean basins. Nevertheless, the deep sea is in motion. Flow in the deep sea is initiated where the normal, density layered, oceanic water column breaks down and surface water sinks due to processes which raise its density. The primary cause of water column destabilization is extreme cooling over a large depth range combined with sea-ice formation. The formation of ice leaves behind a brine which is salty and thus dense. The brine heads for the deep sea. It supplies the great deep ocean water masses, the North Atlantic Deep Water and the Antarctic Bottom Water. On the contrary, the melting of ice increases the fresh water and decreases the salinity levels, having possible implications for ice sheet stability and sea level rise [106, 107].

The West Antarctic ice sheet contains enough water to raise the global sea level by ≈ 5 m if the water were to melt into the ocean [3, 108]. Thus, it is important to investigate the causes of the significant volume loss in the ice sheet in the Amundsen Sea¹ sector observed in recent years [107–110]. In [107, 111] it was observed that the main reason for sea ice decline appears to be warm ocean currents melting the ice from below during their circulation. Forcing mechanisms related to the origin of this warm deep water are benthic Ekman transport [112] and surface wind forcing [113, 114]. This correlation between surface winds and deep current velocities measured in the Amundsen Sea area is the main topic of research in Papers B and C.

This chapter summarizes the concepts and methods necessary to understand the studies

¹See Figure 1 of Paper B or Figure 2 of Paper C for a map of the Amundsen Sea region.

performed in Papers B and C and presents a brief overview of the main results of both works. It is divided in the following manner: Section 4.1 reviews some theoretical background in oceanography; Section 4.2 presents the factors affecting the circulation of deep currents; Section 4.3 presents data and methods used to evaluate the correlation between surface winds and deep currents used in Papers B and C; and Section 4.4 summarizes the main findings of Papers B and C.

4.1 Review of key concepts on ocean circulation

4.1.1 Ekman transport

Due to the Earth's rotation, the flow direction of an ocean current changes along the water depth. This phenomenon, referred to as the Ekman spiral, explains why a wind driven surface current flows to the right of the wind direction in the Northern Hemisphere and to the left of the wind direction in the Southern Hemisphere.

The simplest mathematical model that describes the Ekman spiral can be expressed by [13, 115]

$$fv + A_z \frac{\partial^2 u}{\partial z^2} = 0 \quad (4.1)$$

$$-fu + A_z \frac{\partial^2 v}{\partial z^2} = 0 \quad (4.2)$$

where A_z is the vertical eddy viscosity coefficient and f is the Coriolis parameter defined as

$$f = 2\Omega \sin \Phi \quad (4.3)$$

where $\Omega = 2\pi/(\text{sidereal day}) = 7.292 \times 10^{-5} \text{ s}^{-1}$, and Φ is the latitude.

Assuming that the ocean has infinite dimensions and no variations in density, simple solutions to eqs. (4.1) and (4.2) can be found. In particular, if a 10 m wind is assumed to flow along the $-v$ direction in the southern hemisphere the solutions are

$$u = V_0 \exp\left(\frac{\pi}{D_E} z\right) \cos\left(-\frac{\pi}{4} - \frac{\pi}{D_E} z\right) \quad (4.4)$$

$$v = V_0 \exp\left(\frac{\pi}{D_E} z\right) \sin\left(-\frac{\pi}{4} - \frac{\pi}{D_E} z\right) \quad (4.5)$$

where D_E is the depth of the Ekman layer² given by

$$D_E = \sqrt{\frac{2\pi^2 A_z}{f}} \quad (4.6)$$

²The Ekman depth is functionally defined as the depth at which the current velocity is opposite to the velocity at the surface [115].

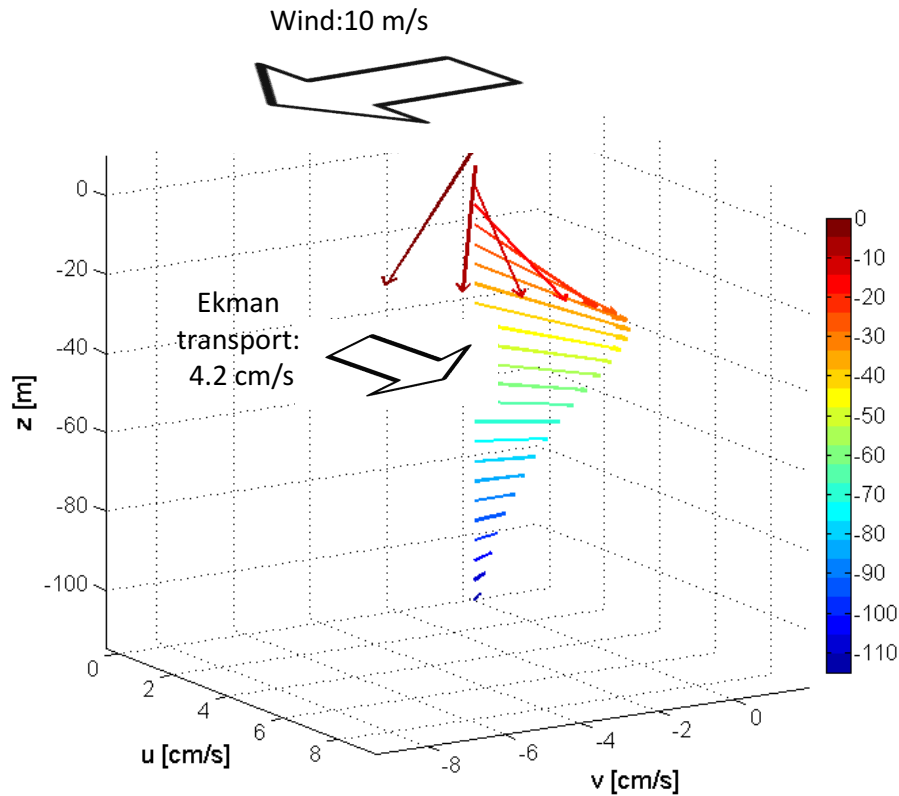


Figure 4.1: Ekman spiral generated by $U_{10} = 10$ m/s at $\Phi = -68^\circ$ latitude and eddy viscosity coefficient $A_z = 0.094$ m²/s. This spiral induces an average Ekman's transport in the u direction.

and the surface current V_0 can be approximated by [115]

$$V_0 = \frac{0.0127}{\sqrt{\sin |\Phi|}} U_{10}, \quad |\Phi| \geq 10 \quad (4.7)$$

Figure 4.1 shows an example of the Ekman spiral at the Antarctic for a $U_{10} = 10$ m/s and $A_z = 0.094$ m²/s [116]. Here it can be noticed that the current induced at the surface flows at about 45° to the left of the wind direction. Since each moving layer is deflected to the left of the overlying layer's the average motion of the Ekman layer, or Ekman transport, will be about 90° to the left of the forcing wind, which coincides with the u direction.

4.1.2 Barotropic and baroclinic conditions

Where ocean waters are well mixed and therefore fairly homogeneous, density nevertheless increases with the depth because of compression caused by the weight of the overlying water. Under these circumstances, the surfaces of equal pressure (isobaric surfaces) are parallel not only to the sea surface but also to the surfaces of constant density (isopycnic surfaces). Such conditions are described as barotropic (see Fig. 4.2(a)) [80].

The hydrostatic pressure at any given depth in the ocean is determined by the density of the overlying sea water. In barotropic conditions, the variation of pressure over a horizontal surface

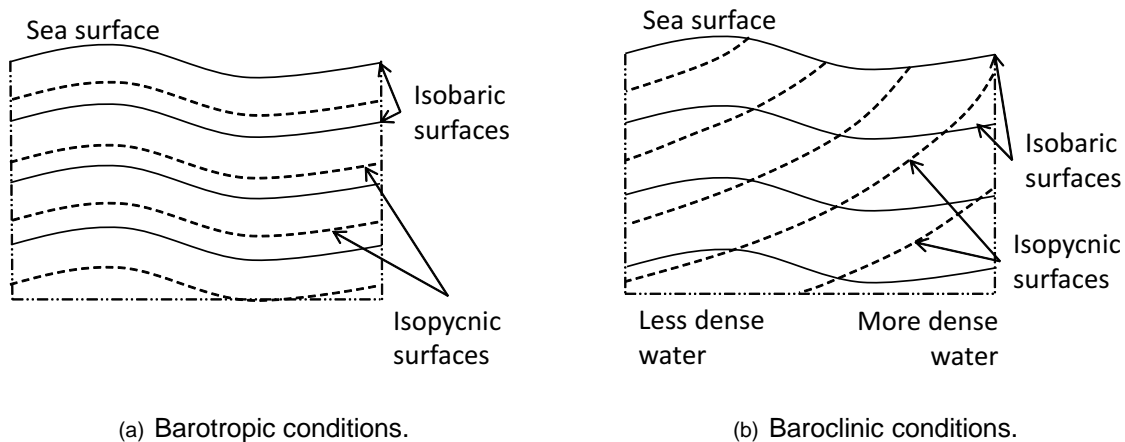


Figure 4.2: Sketch of isobaric (constant pressure) and isopycnic (constant density) surfaces in barotropic and baroclinic conditions.

at depth is determined only by the slope of the sea surface, which is why isobaric surfaces are parallel to the sea surface. In a fluid that is not all of the same density, the isopycnic surfaces and the isobaric surfaces are not aligned (see Fig 4.2(b)). For these flows, the measurement of the misalignment between the gradient of the pressure with respect to the gradient of the density is called baroclinity [80, 117].

In baroclinic flows the velocity and density vary rapidly in the vertical, especially near the surface layers; such motions are typically of much lower frequency and propagate more slowly than the barotropic flows, which are essentially uniform throughout the water column [13].

4.1.3 Upwelling and downwelling

The rising of water to compensate for the seaward surface flow is called upwelling. Thus, the Ekman transport is a factor in coastal upwelling [118]. Upwelling is particularly effective around Antarctica because the water column there is uniformly cold, which means that the thermocline barrier to vertical motion is weak and waters can be drawn up from depth. The opposite occurs when the surface waters sinks, called downwelling, which can be due to the surface winds or to an increase in density. Figure 4.3 shows sketches of coastal upwelling (Fig. 4.3(a)) and downwelling (Fig. 4.3(b)) forced by the wind in the Antarctica, where it can be seen that both processes are linked to a bottom flow opposite to the direction of the Ekman transport.

Upwelling in the Southern Ocean provides one of the main avenues by which deep waters eventually surface. Once there, solar warming will lead to decreasing density and a return of water to the upper ocean circulation system. However, upwelling isn't the only way out of the deep sea. Any process which encourages vertical mixing will transfer water out of the depths. Water flowing over variable seabed topography can experience strong mixing, which is

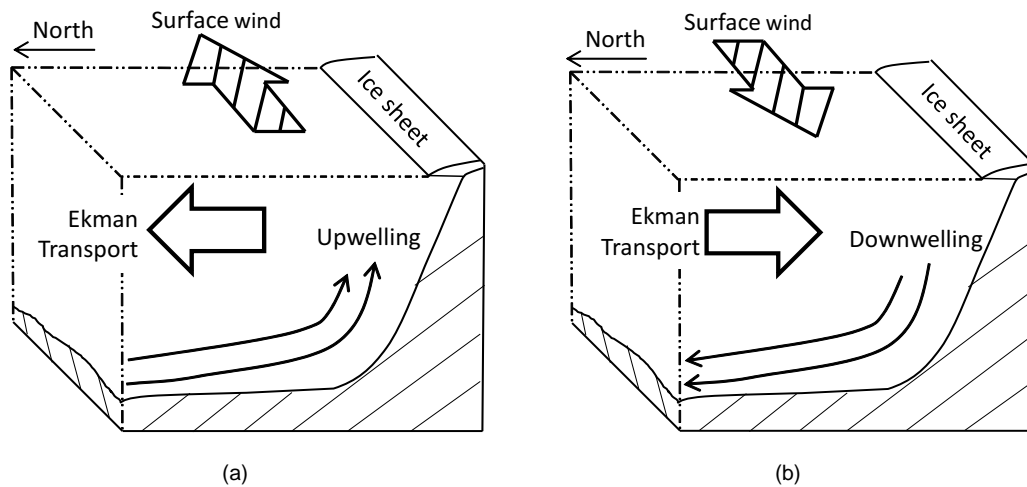


Figure 4.3: Coastal upwelling (a) and downwelling (b) due to surface wind forcing in the Antarctica.

particularly effective where the vertical temperature gradients are weak (limited thermocline). Also, when the sea bottom is rough, the flow of deep currents by itself generates upward motion in the water column [119].

4.2 Factors affecting the deep currents circulation

Deep water, although not affected directly by the wind, is in motion at all depths. Deep water flow gives a third dimension to the ocean's response to the planetary temperature gradient [120]. This cycle is vital to the distribution of heat, chemicals and life in the oceans. In this section several factors that can affect the circulation of deep currents are described.

4.2.1 Temperature and salinity

The deep water currents are commonly referred to as thermohaline circulation. This arises from density differences between water masses produced by variations in water temperature (thermal effect) and salinity (haline effect).

Deep water masses mostly develop at high latitudes. A simplified model depicts the water flow in the oceans as an immense “conveyor belt” (see Fig. 4.4) [121]. This model includes the sinking of waters into the ocean bottom depths at the South East Greenland and in the Atlantic sector of Antarctica. Deep waters born in the Atlantic spread to the other ocean basins through the Antarctic circumpolar current. This seaway serves as the roundabout connecting all the world's oceans and allowing deep Atlantic water to spread ultimately to the Pacific. Along the way water finds return routes to the surface. Since deep waters are more dense than those at the surface, energy has to be used to pump them up. Ultimately, the energy is provided by the

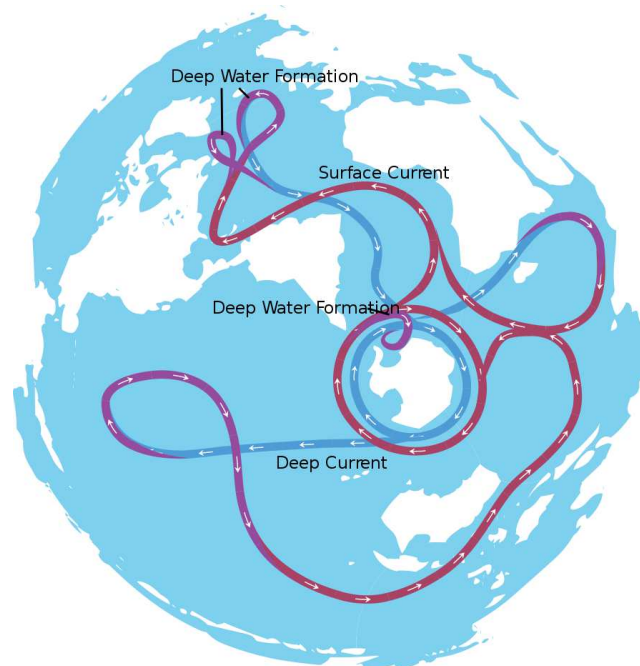


Figure 4.4: The Global conveyor belt describing (in a simplified way) the deep ocean circulation on a continuous-ocean map.

planetary heat gradients as these drive wind and deep ocean flow and the upwelling and mixing of water [105, 121–123].

In [123], it was used the definition of a thermohaline streamfunction. This enabled to estimate the turnover time of the conveyor belt to be between 1000 and 2000 years, depending on the choice of stream layer. However, the concept of “conveyor belt” is a metaphor for the much more complex, three-dimensional, and time-variable circulation now commonly referred to as the overturning circulation. The actual flow paths involved in the global overturning circulation are much more complex, including narrow boundary currents, recirculation gyres, small-scale eddies, and jets. The deep circulation is steered by the topography of the seafloor and can also be influenced by the deep expression of circulation features in the upper ocean, such as boundary currents and eddies [124].

4.2.2 Upslope benthic Ekman transport

The benthic boundary layer is located at the bottom of the oceans [13]. When a barotropic current flows over a solid seabed the Coriolis force induces a stress generating an Ekman transport, equivalent to the one described in Section 4.1.1, in the interface between the bottom of the ocean and the seabed instead of the interface between the ocean surface and the MABL.

When the fluid is vertically stratified and the bottom slopes, the Ekman transport will advect relatively dense fluid up (or down) the slope, which generates buoyancy forces close to the bottom. These buoyancy forces are directed oppositely to the pressure gradient force driving

the overlying barotropic flow [112].

4.2.3 Surface wind

From the Ekman transport theory, surface winds produce an current transport approximately at 90° , to the right in the Northern Hemisphere and to the left in the Southern Hemisphere, at the upper part of the ocean (see Sec. 4.1.1). To compensate for this water displacement at the upper part of the ocean there is an upwelling or a downwelling of water (see Sec. 4.1.3) linked to a flow at the bottom of the ocean. Due to this interaction surface winds may induce deep current circulations.

4.3 Correlation between surface winds and deep currents

4.3.1 Data

Papers B and C of this thesis investigate the variability of the warm deep current in the Amundsen Sea shelf using measurements of a mooring placed at 72.46°S and 116.35°W during 2010 and 2011. The mooring consisted of an Acoustic Doppler Current Profiler (ADCP), with continuous measurements of pressure, salinity, temperature and velocity between 320 m and 540 m depth. In Paper B it was noticed that water at the Amundsen shelf appears to be a mixture between glacier meltwater and source water with temperature between 1°C and 1.4°C and salinity of about 34.73 psu, that is, source water found below the temperature maximum outside the shelf. The deepest shelf water, found at 500-600 m, seemed to come from depths of at least 1000 m off the shelf. Then, following the modeled results from [114, 125], surface wind data from ERA-interim (see Section 3.5.3) were correlated with the registered deep water velocities to investigate surface winds as a possible source of deep current variability.

Since the results of Paper B (see Section 4.4), although statistically significant, showed low values for the correlation, Paper C made a further evaluation of the correlation between surface winds and deep water velocities during the months with lower ice coverage. For this evaluation both SAR derived surface winds (see Section 3.4) together with the ones from ERA-interim were considered taking into account their geographical distribution. SAR wind data were considered due to its inherent higher (10 km wind cells) resolution than the model wind vector estimates (≈ 50 km resolution in latitude). However, the wind directions were obtained from ERA-interim data instead of the wind direction retrieval method developed in Paper A. These modeled wind directions were used after an empirical analysis that showed that the streak features necessary to determine the wind directions from the SAR data were often not present, presumably due to stable conditions in the MABL.

4.3.2 Method

The mooring data registered deep water velocities in the Amundsen Sea trough. In order to account for most of their variability the tidal effects were removed [126] and the data were decomposed into Empirical Orthogonal Function (EOF) modes [127]. This decomposition was carried out with the first mode (EOF1) explaining 90% of the variability and the second mode (EOF2) explaining 7% of the variability. Both modes were correlated to different forcing mechanisms, with EOF1 coupled to a barotropic response and EOF2 coupled with a baroclinic response in the water column.

The correlation was computed as an estimate of the covariance between two time series, y_{1t} and y_{2t} , at lags $k = 0, \pm 1, \pm 2, \dots$

$$c_{y_1, y_2}(k) = \begin{cases} \frac{1}{T} \sum_{t=1}^{T-k} (y_{1t} - \bar{y}_1)(y_{2, t+k} - \bar{y}_2) & k = 0, 1, 2, \dots \\ \frac{1}{T} \sum_{t=1}^{T+k} (y_{2t} - \bar{y}_2)(y_{1, t-k} - \bar{y}_1) & k = 0, -1, -2, \dots \end{cases} \quad (4.8)$$

where \bar{y}_1 and \bar{y}_2 are the sample means of the series.

The sample standard deviations of the series are $s_{x_i} = \sqrt{c_{x_i x_i}(0)}$. Thus, the estimate of the cross correlation is:

$$r_{y_1 y_2}(k) = \frac{c_{y_1 y_2}(k)}{s_{y_1} s_{y_2}} \quad k = 0, \pm 1, \pm 2, \dots \quad (4.9)$$

In Paper B daily and monthly averages of mooring velocities and temperature were correlated with surface winds from the ERA-interim model for the time series between 2010 and 2011. In terms of eqs. (4.8) and (4.9) the time series y_{1t} was given by the eastward component of the wind from the ERA-interim model averaged over the Amundsen Sea area (68°S to 73°S and 100°W to 130°W). y_{2t} was alternatively defined as: the along-trough (u) component of the EOF1 mode (u_{EOF-m1}), the across trough component (v) of the EOF1 mode (v_{EOF-m1}), the bottom temperature (T_{BOT}) or the heat transport (Q_H).

In Paper C the evaluation of the correlation follows a different approach. In this case the Amundsen Sea region was spatially divided into $M \times N$ locations. For each of these locations there were time series of the surface winds, derived from both ERA-interim model and SAR wind speed estimates. In this Paper the ice covered surface in the Amundsen Sea area was also considered, and masked out from the surface wind estimates. The ice coverage was also taken into account in the selection of the time series length. Thus, there were two time series, one for 2010 and another for 2011, during the months with minimum ice coverage. The correlation was then evaluated between each of the $M \times N$ time series associated with the geographical location of the surface wind from both ERA-interim and SAR data with u_{EOF-m1} and v_{EOF-m1} .

4.4 Results

The results from Paper B indicated that u_{EOF-m1} had a statistically significant correlation with the surface winds, with a maximum value of 0.41 with a lag of about 2 days. However there was no correlation between the temperature and thickness of the warm current layer with the surface winds.

The observational data of Paper B contradicted the modeled results from [114, 125] in two aspects. First, the modeled seasonal variation of the warm-layer thickness had a pronounced maximum in September-November, while the mooring measurements presented this maximum during March-May. Second, this paper didn't find a correlation between the layer thickness and the eastward wind, which had a large variability during the the whole period.

The relatively low value of the maximum correlation between the winds and currents of Paper B motivated the approach used in Paper C. Here the high resolution of the SAR wind maps were used to interpret two events (one in 2010 and one in 2011) in the ocean current direction. In 2010, with a low ice coverage, there was a rapid response of the current variation with respect to the wind field. In 2011, with larger ice coverage, the influence of the wind in the current variation presented a larger delay.

In Paper C the correlations and delays between the easterly component of the surface winds and the mooring EOF1 velocities were, as expected, found to be statistical significant for u_{EOF-m1} . In both years the results had different values and time delays, according to their geographical location, indicating a shift of the forcing region. The results pointed to a quite complex interaction between the datasets during 2010, with both positive and negative correlations and time delays statistically significant for u_{EOF-m1} . In 2011, the location and correlation of the source wind were more explicitly defined, with a maximum correlation of 0.71 and a time lag of 10 days. It is hypothesised that the difference between the results in 2010 and 2011 are mainly due to the influence of the ice coverage variation of both years.

Further work requires the evaluation of benthic Ekman transport induced by deep reaching currents along the continental slope of the Amundsen Sea as an alternative source of forcing for the warm deep currents melting the ice shelves.

Surface current retrieval from infrared radiometry

The relatively large coastline of Sweden (3218 km) brings interest in the monitoring of the surface currents in its surrounding waters (Baltic Sea, Kattegat and Skagerrak). The embedded distribution of these waters seems to be a possible application of coastal HF radars. However, the brackish tendency of these waters, with salinity levels of 0.3-0.5 psu in the northern parts of the Baltic Sea area, restricts their applicability [36, 128]. Thus, satellite monitoring of surface currents around Sweden is an alternative of interest.

In chapter 2, which reviewed sensors used in satellite oceanography, it was mentioned that SAR surface current retrievals, although at high resolution, so far are restricted to the detection of only one component of the current field (see section 2.1.1). Moreover the geostrophic current retrieval with altimeter sensors provides very coarse resolutions (see section 2.1.3). Hence, the possibility of surface current retrieval from infrared (IR) radiometer sensors (see section 2.2.1) is an alternative of interest.

The routine derivation of infrared brightness temperature or sea surface temperature (SST) has been used to estimate the surface circulation by calculating the motion of thermal features (coastal upwellings, filaments, or eddies) in successive images. Velocity was first estimated interactively in a sequence of images by tracking features visually [129–132]. The results were not reproducible by different operators and the method was impractical for the routine analysis of large datasets. Thus, objective and automated feature-tracking methods were developed by using different criteria such as gradient thresholds [133] or wavelets [134]. These methods usually require extensive image preparation and considerable user input to determine the criteria that define certain features. Other more straightforward methods match patterns (points, borders, or regions) in all possible subwindows of one image with those in the subsequent one. In this context, the maximization of the normalized cross-correlation (NCC) coefficient, which is known as the maximum cross-correlation (MCC) technique, is the most popular region-based

matching strategy applied to compute ocean circulation [135–151]. This technique is used in Paper D to estimate current fields around Sweden and is compared with surface current data from a weather prediction model.

This chapter summarizes the concepts, methods and main results of the MCC current retrieval developed for Paper D. It is divided as follows: Section 5.1 reviews the theoretical background behind the MCC current estimation; Section 5.2 describes the methodology of the implementation; Section 5.3 describes the data used; and Section 5.4 summarizes the results of the method evaluation.

5.1 Brightness temperature of the ocean surface

Most of the solar radiation is received by the water surface that covers 71% of the Earth’s surface. As a result of its heat capacity and circulation, the ocean has the ability to both store and redistribute its heat before it is released to the atmosphere. At its surface the skin temperature (to depth of a fraction of a mm) can be different from that a few centimeters beneath the surface. This is due to the combined effects of evaporation, sensible heat transfer and radiative energy exchange [34]. Because this layer is extremely thin, it is most reliably sampled by a remote sensing method.

In section 2.2.1 it was explained that IR sensors measure the brightness temperature of objects. For the ocean surface the measured radiance, B_s , for a particular angle of observation, θ , depends of the emissivity of the sea water, $\epsilon_s(\theta)$, and the downwelling sky radiation. The radiances are related to the surface temperature, T_s and the atmospheric temperature, T_a , by Planck’s law (eq. 2.6). Thus [34]

$$B_s = \epsilon_s(\theta)B(T_s, \theta) + (1 - \epsilon_s(\theta))B(T_a, \theta) \quad (5.1)$$

where $B(T_a, \theta)$ is the downwelling radiance from the sky. Here it is assumed that there is specular reflection of the sky radiation at the surface and there is no absorption between the radiometer and the ocean surface. For incidence angles less than 60° the emissivity of the ocean surface is well known, and is relatively independent of the surface wind speed and the sea state, although it varies with respect to the wavelength [152].

Using satellite imagery to measure surface water movement assumes that the thermal feature, representing the temperature of a volume of water, remains relatively intact during the sampling interval. However, there are physical and biological processes that can be discussed by examining a simplified equation for the conservation of heat at the surface of the ocean [138, 140]

$$\frac{dT}{dt} = K_h \nabla_h^2 T + K_z \frac{\partial^2 T}{\partial z^2} + \sum_i Q_i \quad (5.2)$$

where $\frac{dT}{dt}$ is the derivative of temperature T over time t , K_h and K_z are the horizontal and vertical diffusivity, and Q_i is the heating source (or sink) term.

The variation term $\frac{dT}{dt}$ can also be expressed as

$$\frac{dT}{dt} = \frac{\partial T}{\partial t} + \mathbf{V}_h \cdot \nabla_h T \quad (5.3)$$

where \mathbf{V}_h represents the fluid velocity.

For a two-dimensional, non-compressible flow, assuming a well mixed layer ($\frac{\partial T}{\partial z} \ll \frac{\partial T}{\partial x}$) and ($\frac{\partial T}{\partial z} \ll \frac{\partial T}{\partial y}$), the combination of eqs. (5.2) and (5.3) becomes [140]

$$\frac{\partial T}{\partial t} = -\mathbf{V}_h \cdot \nabla_h T + K_h \nabla_h^2 T + \sum_i Q_i \quad (5.4)$$

where the first term, $-\mathbf{V}_h \cdot \nabla_h T$, is the advection term, the second term, $K_h \nabla_h^2 T$, is the horizontal diffusion term and the last term $\sum_i Q_i$ represents the sea-air interaction.

Assuming that the diffusivity and the heating source can be neglected, the surface current flow can be described by the advection term as [138]

$$\frac{\partial T}{\partial t} + u \frac{\partial T}{\partial x} + v \frac{\partial T}{\partial y} = 0 \quad (5.5)$$

where u and v are the velocity components of the surface current field.

The MCC method assumes a surface current flow described by the advection variation of eq. (5.5). Wahl and Simpson [153] found that horizontal diffusion has a minor effect on surface feature character for periods less than 24 hours, while in [138] it was postulated that non-advective processes as air-sea interaction, vertical mixing and rotation are the more significant processes which can alter the feature over time.

The nature of the MCC technique necessitates the existence of suitable thermal or color features for making the current measurements [132]. Therefore monitoring surface flow from infrared radiometry images is possible only in regions with heterogeneous mesoscale surface thermal or color patterns. The trackable features must also preserve their identity from one image to the next. The extent to which the features preserve their shape greatly affects tracking precision and hence the accuracy of the measurements. Clearly, the closer in time the two images are recorded the less the features will have changed. However, the error due to imprecise tracking increases as the time separating the two images decreases.

5.2 Maximum cross correlation method

The essence of the MCC algorithm lies in locating a small subscene from a first image inside another image from the same region. It is done by computing a cross correlation between the subscene and the correspondingly sized area in the second image moved over a predefined search area until a maximum correlation is found [136].

The algorithm divides the first image into a number of template windows (see Fig. 5.1) according to the oceanic features to be resolved. Each of these templates is searched for in a

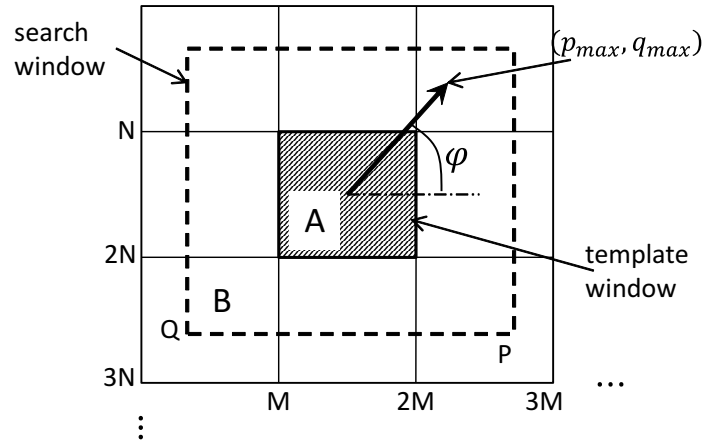


Figure 5.1: Sketch of division of template and search windows for the MCC computation. The vector indicates the offset corresponding to a maximum cross correlation.

second image inside a search window of size depending of the maximum current speed expected between the two sequential images.

Important parameters that should be carefully considered when using this method are the size of the template window A , and the velocity resolution that can be achieved. The size of A represents a balance between having sufficient features to track in the template and smoothing the resultant vector flow field [36]. Larger template windows result in a smoother flow field, whereas small template sizes will allow tracking of finer features, giving a less homogeneous flow field. In order to consider only reliable velocities a correlation cutoff larger than zero may be selected. The velocities that can be resolved by this method are determined by the image pixel size and the time between successive images [139].

Having a template matrix A of $M \times N$ and a search area B of $P \times Q$, the normalised spatial cross correlation at a spatial lag p and q is defined by

$$\begin{aligned} r(p, q) &= \frac{1}{N \cdot M} \cdot \frac{1}{\sigma_A \sigma_B} \sum_{x=0}^{M-1} \sum_{y=0}^{N-1} [A(x, y) - \bar{A}(x, y)] [B(x+p, y+q) - \bar{B}(x+p, y+q)] \\ &= \frac{1}{N \cdot M} \cdot \frac{\text{Cov}(p, q)}{\sigma_A \sigma_B} \end{aligned} \quad (5.6)$$

where σ_A and σ_B are the standard deviations of the template A and the search window B , respectively. The summation is performed over all values of x and y which make up the template window. \bar{A} and \bar{B} stand for the mean values of the windows. $\text{Cov}(p, q)$ is the covariance of the lags in the p (x direction) and q (y direction). The relative displacement (p, q) between the template and the search windows of the sequential scenes when the cross correlation has its maximum value determines the advective velocity vector. In this way the displacement speed c and its direction φ can be computed by

$$c = \frac{\sqrt{(p_{max} \Delta x)^2 + (q_{max} \Delta y)^2}}{\Delta t} \quad (5.7)$$

$$\varphi = \arctan \left(\frac{q_{max} \Delta y}{p_{max} \Delta x} \right) \quad (5.8)$$

5.3 Data

5.3.1 AVHRR

Infrared images from Advanced Very High Resolution Radiometer (AVHRR/3) sensors at level 1b have been used in the evaluation of the MCC method of Paper D. The data has been provided through the Comprehensive Large Array-data Stewardship System (CLASS) from the National Oceanic and Atmospheric Administration (NOAA) [154].

Currently there are AVHRR/3 sensors on the NOAA-15, 16, 17, 18, 19 and MetOp-A/B satellites. The orbits are timed to allow each satellite to have complete global coverage twice per day (normally a daytime and a nighttime view of the earth) in swaths of about 2,600 km in width. AVHRR/3 level 1b data are grouped into four data types to: HRPT (High Resolution Picture Transmission, 1.1 km, at U.S. and coastal areas), LAC (Local Area Coverage, 1.1 km, outside the U.S), FRAC (Full Resolution Area Coverage, 1.1 km, on Metop satellites) and GAC (Global Area Coverage, 4 km). Due to their higher resolution, HRPT, LAC, and FRAC have been considered for the surface current retrieval with the MCC method. With this pixel resolution areas of 10 and 20 km resolution have been considered as having statistical significance for the retrieval of advective surface velocities.

5.3.2 HIROM-B

Data from the High Resolution Operational Model for the Baltic Sea (HIROM-B), from the Swedish Meteorological and Hydrological Institute (SMHI) [155], have been used for comparison with the MCC results of Paper D.

The HIROM-B model data used have outputs with 24 h UTC forecast. It represents a 3-dimensional baroclinic model of the North Sea and the Baltic Sea, designed for daily operational use. The model is mainly forced by SMHI's operational atmospheric model (HIRLAM), but also by river runoff from an operational hydrological model and wave radiation stress from a wind wave model [155]. The data used was provided with a resolution of 2 nautical miles (3.7 km) covering Skagerrak, Kattegat and the Baltic Sea area.

5.4 MCC evaluation

Despite the age of the MCC algorithm and the development of more recent techniques that can be used for surface current retrieval from satellite data, its replacement has not yet been

recognized. Thus, Paper D includes the results from the implementation and evaluation of the MCC method applied to water surfaces around Sweden.

It is essential for the success of the MCC technique that the two images of the pair are coregistered as accurately as possible. A rotation between the images reduces the matching coherency, and a translational shift produces spurious derived fields. In Paper D the images were corrected by using standard Mercator map projection with 100 automatically selected control points and the global datum WGS-84. In a second stage the images were resampled using cubic convolution to a pixel size of 1 km. Furthermore, land pixels were masked out and set to zero. Pixels affected by cloud, fog or other aerosols were detected and also set to zero. This detection was based on their higher brightness temperature with respect to the median temperature of the image after land masking.

The evaluation of the MCC method in the study case of Paper D indicated surface currents on average lower than 50 cm/s with a variable agreement with the HIROM-B current estimates depending of the resolution of the retrievals. Thus, the current fields detected with images close in time (about 3 h) had in most cases a similar magnitude than the ones derived from the HIROM-B model. However, there existed small discrepancies in the localization of the large current values which could be due to the observation of circulation patterns not predicted by the model or due to errors in the MCC retrievals.

As shown in eq. (5.2) several processes can affect the accuracy of the MCC results. The currents generated by tidal variations in the Baltic Sea are usually small, with tidal ranges lower than 0.5 m, because it is connected with the Atlantic basin only by the narrow strait of the Belt Sea and Kattegat [21, 36]. Without the presence of wind, inertia currents, generated by the curved motion of the water due to the Coriolis force, are usually present in the Baltic Sea [80]. For surface wind speeds less than 10 m/s, horizontal as well as vertical diffusion, air-sea heat exchanges are the dominant processes in the variation of surface temperatures. Surface winds greater than 20 m/s usually cause intense vertical mixing, destroying the thermal feature. Additionally, diurnal heating may also cause significant distortion of thermal features by wind stress induced diurnal jets which transport surface thermal features normal to wind direction at velocities up to 0.1 m/s for moderate winds [140]. Therefore, further work is necessary to understand and set limits to the validity of the MCC current estimates in the Baltic Sea.

Conclusions and outlook

This thesis focuses on the development, evaluation and assessment of an algorithm for surface wind retrieval with satellite C-band synthetic aperture radar (SAR) data, an application of SAR derived surface winds for oceanography, and the evaluation of an algorithm for surface currents retrieval with infrared (IR) radiometry data.

The wind speed retrieval with SAR data was achieved with the inversion of geophysical model functions (CMOD-IFR2, CMOD5 and CMOD5.N) using wind direction data obtained in two ways, from the analysis of features in the SAR image or from a weather prediction model. The results based on SAR derived wind directions, which included the contribution of a regularization method, were validated against in-situ measurements. For this validation the best performance was obtained for offshore regularized wind directions using CMOD5.N, with bias and standard deviation of 9° and 25° for the wind directions, and -0.1 m/s and 1.4 m/s for the wind speeds. A significant contribution of this work was the assessment of the SAR derived wind directions at different resolutions with respect to the reference data at coarser resolutions. It was found that, when wind directions were obtained from the SAR data, the agreement with the reference data improves for coarser SAR wind direction retrievals. Thus, the detection of small scale features benefits from the wind direction retrieval from SAR data.

The retrieval of wind directions from SAR images for oceanography in polar regions is limited by the stability of the marine atmospheric boundary layer (MABL). A stable MABL, often the case for water surfaces colder than their overlying air, does not show signatures for the wind direction retrieval normally produced by convection in the form of boundary layer rolls. Therefore, wind directions from a weather prediction model were used for SAR wind retrieval in the Amundsen Sea, Antarctica. This application put in evidence that SAR derived wind speeds can be correlated with deep water velocities and present higher resolution and correlation values than equivalent evaluations with wind data purely derived from a weather model. This correlation can be interpreted as a possible explanation for the presence of warm deep currents which have been observed to melt the ice shelves in Antarctica from below, and

could have effects on the general ocean circulation and sea level rise.

A future improvement of the SAR wind retrieval algorithm will be an adaptive selection of wind directions from either the SAR image or a weather model, based on the evaluation of features in the SAR image. With this, both the advantage of SAR fine wind resolutions and model data availability will be taken into account. This improvement can also be of great advantage in coastal areas, where the performance of the present implementation is reduced. Another alternative will be the use of recent developments on cross-polarized backscattering models for fully polarimetric SAR data, from which the wind speeds can be derived. With this, the wind direction retrieval will have both the use of geophysical model functions and the detection of the wind aligned features (normally present in neutral and unstable conditions of the MABL) as alternatives for its derivation. Furthermore, the recent and future availability of satellite data from L-band and X-band SAR sensors, combined with new developments on geophysical model functions for these frequencies, can also be used to expand the applicability of the algorithm for SAR surface winds retrieval developed in this thesis.

So far the maximum cross correlation (MCC) algorithm, implemented for surface current retrievals with IR data, has only been compared with model estimates in selected examples. The results indicated comparable current fields for evaluations in cloud free days and time delays of about 3 h between the pair of IR images used as a source for the surface current retrieval. However, the influence of diverse physical processes (e.g. diurnal temperature variations, tides, inertia currents) has still to be taken into consideration and a validation against in-situ data is still to be done. Therefore, future work will include the statistical comparison of the current estimates with respect to model and in-situ data for different time delays of the IR input data and different correlation thresholds. With this it is expected to establish a protocol dictating the applicability and limitations of the MCC current retrieval algorithm in the surface waters surrounding Sweden, with the expectation of a future assimilation into weather prediction models.

Future improvements of surface current retrievals might use other techniques and sensors. Promising candidates are in particular SAR techniques that use Doppler shift velocity information, such as along-track interferometry (ATI), and Doppler centroid anomaly analysis. These techniques were not considered for the work in this thesis due to lack of data and the restriction of the measurements which provide only one component of the current field. Nevertheless, these techniques are still of great interest due to their capabilities of measuring surface currents in spatial resolutions of 0.5 to 10 km.

Acknowledgements

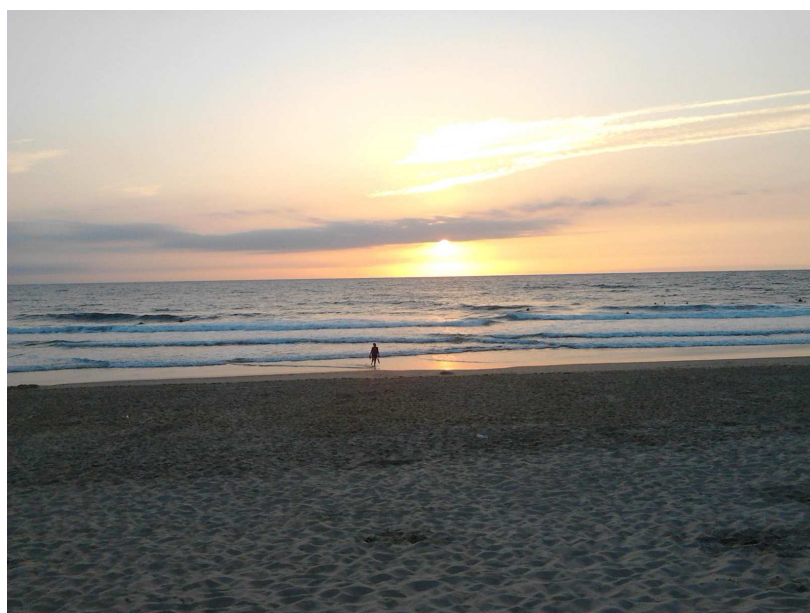
First of all, I would like to thank my supervisors Lars Ulander and Leif Eriksson for giving me the opportunity to do this PhD work, for their advices, support, help and patience. The other members of the Radar Remote Sensing group – Anders, Annelie, Gustaf, Hanna, Jan, Maciej, and Malin – should also be acknowledged for helpful discussions and a nice reception at work.

I would also like to thank the rest of the people that I have met at the Department of Earth and Space Sciences, in particular Claudia, Donal, Jo, Jörg, Kristell, Maria, Maryam, Mattias, Monica, Ole Martin, Sagi, Santiago, Sini, Susana, Vladimir, Yan, among many others. They have made of Gothenburg a nice place not only to work, but for living in general.

A special thank also to my collaborators at the Universities of Gothenburg and Miami. In particular I want to thank Anna Wåhlin for the productive discussions we have held and for her enthusiasm.

Financial support for this work is acknowledged to various projects with the Swedish National Space Board and the European Commission.

Last but not least, I would like to thank my parents Mirtha and Andrés, my sisters María Inés and Cecilia, and my friends in Venezuela, who helped me, took care of me, and always have supported me during my decisions in life.



Bibliography

- [1] J.L. Sarmiento, T.M.C. Hughes, R.J. Stouffer, and S. Manabe, “Simulated response of the ocean carbon cycle to anthropogenic climate warming,” *Nature*, vol. 393, no. 6682, pp. 245–249, 1998.
- [2] A.C. Manning and R.F. Keeling, “Global oceanic and land biotic carbon sinks from the scripps atmospheric oxygen flask sampling network,” *Tellus, Series B: Chemical and Physical Meteorology*, vol. 58, no. 2, pp. 95–116, 2006.
- [3] N.L. Bindoff, J. Willebrand, V. Artale, A. Cazenave, J. Gregory, S. Gulev, K. Hanawa, C. Le Quéré, S. Levitus, Y. Nojiri, C.K. Shum, L.D. Talley, and A. Unnikrishnan, *Climate Change 2007: The Physical Science Basis. Contribution of Working Group I to the Fourth Assessment Report of the Intergovernmental Panel on Climate Change*, chapter Observations: Oceanic Climate Change and Sea Level, pp. 386–432, Cambridge University Press, 2007.
- [4] P. Burgherr, “In-depth analysis of accidental oil spills from tankers in the context of global spill trends from all sources,” *Journal of Hazardous Materials*, vol. 140, no. 1-2, pp. 245–256, 2007.
- [5] J. Brodie, R.A. Andersen, M. Kawachi, and A.J.K. Millar, “Endangered algal species and how to protect them,” *Phycologia*, vol. 48, no. 5, pp. 423–438, 2009.
- [6] M.-I. Roh, “Determination of an economical shipping route considering the effects of sea state for lower fuel consumption,” *International Journal of Naval Architecture and Ocean Engineering*, vol. 5, no. 2, pp. 246–262, 2013.
- [7] GCOS-107, “Systematic observation requirements for Satellite-based products from climate,” Tech. Rep., World Meteorological Organization & United Nations Environment Program, 2006.

- [8] I. Robinson, *Measuring the Oceans from Space: The principles and method of satellite oceanography*, Springer and Praxis Publishing UK, 2004.
- [9] V. Barale, J.F.R. Gower, and L. Alberotanza, Eds., *Oceanography from Space*, Springer, 2010.
- [10] I. Robinson, *Discovering the Oceans from Space: The unique applications of satellite oceanography*, Springer and Praxis Publishing UK, 2010.
- [11] M.I. Skolnik, *Introduction to radar systems*, Mc Graw Hill, 3rd edition, 2001.
- [12] R.J. Sullivan, *Radar foundations for imaging and advanced concepts*, Scitech Publishing, 2004.
- [13] J.R. Apel, *Principles of Ocean Physics*, vol. 38 of *International Geophysics*, Academic Press, 1990.
- [14] F.T. Ulaby, R.K. Moore, and A.K. Fung, *Microwave remote sensing: active and passive: Radar Remote Sensing and Surface Scattering and Emission Theory*, vol. II, Addison-Wesley, Advanced Book Program, 1982.
- [15] R.M. Goldstein and H.A. Zebker, “Interferometric radar measurement of ocean surface currents,” *Nature*, vol. 328, no. 6132, pp. 707–709, 1988.
- [16] R. Romeiser and H. Runge, “Theoretical evaluation of several possible along-track InSAR modes of TerraSAR-X for ocean current measurements,” *IEEE Transactions on Geoscience and Remote Sensing*, vol. 45, no. 1, pp. 21–35, 2007.
- [17] B. Chapron, F. Collard, and F. Ardhuin, “Direct measurements of ocean surface velocity from space: Interpretation and validation,” *Journal of Geophysical Research C: Oceans*, vol. 110, no. C07008, pp. 1–17, 2005.
- [18] J.A. Johannessen, B. Chapron, F. Collard, V. Kudryavtsev, A. Mouche, D. Akimov, and K.-F. Dagestad, “Direct ocean surface velocity measurements from space: Improved quantitative interpretation of Envisat ASAR observations,” *Geophysical Research Letters*, vol. 35, no. L22608, pp. 1–6, 2008.
- [19] S. Hasselmann, C. Brüning, K. Hasselmann, and P. Heimbach, “An improved algorithm for the retrieval of ocean wave spectra from synthetic aperture radar image spectra,” *Journal of Geophysical Research: Oceans*, vol. 101, no. C7, pp. 16615–16629, 1996.
- [20] C. Mastenbroek and C.F. De Valk, “A semiparametric algorithm to retrieve ocean wave spectra from synthetic aperture radar,” *Journal of Geophysical Research C: Oceans*, vol. 105, no. C2, pp. 3497–3516, 2000.

- [21] D. Park, Ed., *Waves, Tides and Shallow-Water Processes*, Butterworth-Heinemann & The Open University, 2nd edition, 2008.
- [22] S. Lehner, J. Schulz-Stellenfleth, B. Schättler, H. Breit, and J. Horstmann, “Wind and wave measurements using complex ERS-2 SAR wave mode data,” *IEEE Transactions on Geoscience and Remote Sensing*, vol. 38, no. 5, pp. 2246–2257, 2000.
- [23] J. Schulz-Stellenfleth, S. Lehner, and D. Hoja, “A parametric scheme for the retrieval of two-dimensional ocean wave spectra from synthetic aperture radar look cross spectra,” *Journal of Geophysical Research C: Oceans*, vol. 110, no. C05004, pp. 1–17, 2005.
- [24] J. Schulz-Stellenfleth, T. Knig, and S. Lehner, “An empirical approach for the retrieval of integral ocean wave parameters from synthetic aperture radar data,” *Journal of Geophysical Research C: Oceans*, vol. 112, no. C03019, pp. 1–14, 2007.
- [25] W. Alpers, “Theory of radar imaging of internal waves,” *Nature*, vol. 314, no. 6008, pp. 245–247, 1985.
- [26] J. Xue, H.C. Graber, B. Lund, and R. Romeiser, “Amplitudes estimation of large internal solitary waves in the mid-atlantic bight using synthetic aperture radar and marine X-band radar images,” *IEEE Transactions on Geoscience and Remote Sensing*, vol. 51, no. 6, pp. 3250–3258, 2013.
- [27] N. Kozlenko and M.O. Jeffries, “Bathymetric mapping of shallow water in thaw lakes on the north slope of Alaska with spaceborne imaging radar,” *Arctic*, vol. 53, no. 3, pp. 306–316, 2000.
- [28] A. Pleskachevsky, S. Lehner, T. Heege, and C. Mott, “Synergy and fusion of optical and synthetic aperture radar satellite data for underwater topography estimation in coastal areas,” *Ocean Dynamics*, vol. 61, no. 12, pp. 2099–2120, 2011.
- [29] M. Gade, W. Alpers, H. Huhnerfuss, H. Masuko, and T. Kobayashi, “Imaging of biogenic and anthropogenic ocean surface films by the multifrequency/multipolarization SIR-C/X-SAR,” *Journal of Geophysical Research C: Oceans*, vol. 103, no. C9, pp. 18851–18866, 1998.
- [30] A.H. Schistad Solberg, G. Storvik, R. Solberg, and E. Volden, “Automatic detection of oil spills in ERS SAR images,” *IEEE Transactions on Geoscience and Remote Sensing*, vol. 37, no. 4, pp. 1916–1924, 1999.
- [31] A.H.S. Solberg, C. Brekke, and P.O. Husy, “Oil spill detection in Radarsat and Envisat SAR images,” *IEEE Transactions on Geoscience and Remote Sensing*, vol. 45, no. 3, pp. 746–754, 2007.

- [32] Y. Hu, K. Stamnes, M. Vaughan, J. Pelon, C. Weimer, D. Wu, M. Cisewski, W. Sun, P. Yang, B. Lin, A. Omar, D. Flittner, C. Hostetler, C. Trepte, D. Winker, G. Gibson, and M. Santa-Maria, “Sea surface wind speed estimation from space-based lidar measurements,” *Atmospheric Chemistry and Physics*, vol. 8, no. 13, pp. 3593–3601, 2008.
- [33] F.T. Ulaby, R.K. Moore, and A.K. Fung, *Microwave remote sensing: active and passive: Microwave Remote Sensing Fundamentals and Radiometry*, vol. I, Addison-Wesley, Advanced Book Program, 1981.
- [34] I.J. Barton and A.J. Prata, “Satellite derived sea surface temperature data sets for climate applications,” *Advances in Space Research*, vol. 16, no. 10, pp. 127–136, 1995.
- [35] I. S. Robinson, *Satellite oceanography. An introduction for oceanographers and remote sensing scientists*, Chichester: Ellis Horwood, 1985.
- [36] V. Barale and M. Gade, Eds., *Remote Sensing of the European Seas*, Springer, 2008.
- [37] P.W. Vachon and F.W. Dobson, “Validation of wind vector retrieval from ERS-1 SAR images over the ocean,” *Global Atmosphere and Ocean System*, vol. 5, no. 2, pp. 177–187, 1996.
- [38] J. Horstmann, S. Lehner, W. Koch, and R. Tonboe, “Computation of wind vectors over the ocean using spaceborne synthetic aperture radar,” *Johns Hopkins APL Technical Digest (Applied Physics Laboratory)*, vol. 21, no. 1, pp. 100–107, 2000.
- [39] P.W. Vachon and F.W. Dobson, “Wind retrieval from RADARSAT SAR images: Selection of a suitable C-band HH polarization wind retrieval model,” *Canadian Journal of Remote Sensing*, vol. 26, no. 4, pp. 306–313, 2000.
- [40] J. Horstmann, W. Koch, S. Lehner, and R. Tonboe, “Wind retrieval over the ocean using synthetic aperture radar with C-band HH polarization,” *IEEE Transactions on Geoscience and Remote Sensing*, vol. 38, no. 5 I, pp. 2122–2131, 2000.
- [41] M. Portabella, A. Stoffelen, and J.A. Johannessen, “Toward an optimal inversion method for synthetic aperture radar wind retrieval,” *Journal of Geophysical Research C: Oceans*, vol. 107, no. C8(3086), pp. 1–13, 2002.
- [42] B.R. Furevik, O.M. Johannessen, and A.D. Sandvik, “SAR-retrieved wind in polar regions - Comparison with in situ data and atmospheric model output,” *IEEE Transactions on Geoscience and Remote Sensing*, vol. 40, no. 8, pp. 1720–1732, 2002.
- [43] J. Horstmann, H. Schiller, J. Schulz-Stellenfleth, and S. Lehner, “Global wind speed retrieval from SAR,” *IEEE Transactions on Geoscience and Remote Sensing*, vol. 41, no. 10, pp. 2277–2286, 2003.

- [44] Y. He, W. Perrie, Q. Zou, and P.W. Vachon, “A new wind vector algorithm for C-band SAR,” *IEEE Transactions on Geoscience and Remote Sensing*, vol. 43, no. 7, pp. 1453–1457, 2005.
- [45] M. Bruun Christiansen, W. Koch, J. Horstmann, C. Hasager, and M. Nielsen, “Wind resource assessment from C-band SAR,” *Remote Sensing of Environment*, vol. 105, no. 1, pp. 68–81, 2006.
- [46] S. Zecchetto and F. De Biasio, “A wavelet-based technique for sea wind extraction from SAR images,” *IEEE Transactions on Geoscience and Remote Sensing*, vol. 46, no. 10, pp. 2983–2989, 2008.
- [47] A. Reppucci, S. Lehner, J. Schulz-Stellenfleth, and S. Brusch, “Tropical cyclone intensity estimate from wide-swath SAR images,” *IEEE Transactions on Geoscience and Remote Sensing*, vol. 48, no. 4, pp. 1639–1649, 2010.
- [48] C.B. Hasager, M. Badger, A. Peña, X.G. Larsén, and F. Bingöl, “SAR-based wind resource statistics in the Baltic Sea,” *Remote Sensing*, vol. 3, no. 1, pp. 117–144, 2011.
- [49] P.W. Vachon and J. Wolfe, “C-band cross-polarization wind speed retrieval,” *IEEE Geoscience and Remote Sensing Letters*, vol. 8, no. 3, pp. 456–459, 2011.
- [50] X. Yang, X. Li, W.G. Pichel, and Z. Li, “Comparison of ocean surface winds from ENVISAT ASAR, MetOp ASCAT Scatterometer, buoy measurements, and NOGAPS model,” *IEEE Transactions on Geoscience and Remote Sensing*, vol. 49, no. 12, pp. 4743–4750, 2011.
- [51] B. Zhang, W. Perrie, P.W. Vachon, X. Li, W.G. Pichel, J. Guo, and Y. He, “Ocean vector winds retrieval from C-band fully polarimetric SAR measurements,” *IEEE Transactions on Geoscience and Remote Sensing*, vol. 50, no. 11, pp. 4252–4261, 2012.
- [52] T. Shimada, H. Kawamura, and M. Shimada, “An L-band geophysical model function for SAR wind retrieval using JERS-1 SAR,” *IEEE Transactions on Geoscience and Remote Sensing*, vol. 41, no. 3, pp. 518–531, 2003.
- [53] Y. Ren, S. Lehner, S. Brusch, X. Li, and M. He, “An algorithm for the retrieval of sea surface wind fields using X-band TerraSAR-X data,” *International Journal of Remote Sensing*, vol. 33, no. 23, pp. 7310–7336, 2012.
- [54] F.M. Monaldo and R. Beal, *Synthetic Aperture Radar Marine User’s Manual*, chapter 13: Wind Speed and Direction, pp. 305–320, U.S. Dept. of Commerce, NOAA, 2004.

- [55] D.G. Long, R. Scott Collyer, R. Reed, and D.V. Arnold, “Dependence of the normalized radar cross section of water waves on bragg wavelength-wind speed sensitivity,” *IEEE Transactions on Geoscience and Remote Sensing*, vol. 34, no. 3, pp. 656–666, 1996.
- [56] M. Henderson Floyd and J. Lewis Anthony, *Manual of Remote Sensing, Principles and Applications of Imaging Radar*, John Wiley & Sons, Inc., 1998.
- [57] F.J. Wentz, S. Peteherych, and L.A. Thomas, “A model function for ocean radar cross sections at 14.6 GHz,” *Journal of Geophysical Research*, vol. 89, no. C3, pp. 3689–3704, 1984.
- [58] D.G. Long, “Display and computation of winds in oceanography and meteorology,” Tech. Rep. # MERS 90-001, MERS, 1994.
- [59] A. Stoffelen and D. Anderson, “Scatterometer data interpretation: Estimation and validation of the transfer function CMOD4,” *Journal of Geophysical Research*, vol. 102, no. C3, pp. 5767–5780, 1997.
- [60] Y. Quilfen, B. Chapron, T. Elfouhaily, K. Katsaros, and J. Tournadre, “Observation of tropical cyclones by high-resolution scatterometry,” *Journal of Geophysical Research*, vol. 103, no. C4, pp. 7767–7786, 1998.
- [61] H. Hersbach, A. Stoffelen, and S. de Haan, “An improved C-band scatterometer ocean geophysical model function: CMOD5,” *Journal of Geophysical Research*, vol. 112, no. C03006, pp. 1–18, 2007.
- [62] H. Hersbach, “Comparison of C-Band scatterometer CMOD5.N equivalent neutral winds with ECMWF,” *Journal of Atmospheric and Oceanic Technology*, vol. 27, no. 4, pp. 721–736, 2010.
- [63] S. Emeis, *Surface-based remote sensing of the atmospheric boundary layer*, vol. 40 of *Atmospheric and Oceanographic Sciences Library*, Springer Dordrecht, Heidelberg, 2011.
- [64] S. Emeis, *Wind energy Meteorology*, vol. 40 of *Atmospheric and Oceanographic Sciences Library*, Springer Dordrecht, Heidelberg, 2011.
- [65] O. G. Sutton, *Micrometeorology*, McGraw-Hill, 1953.
- [66] E.L. Andreas, “The atmospheric boundary layer over polar marine surfaces,” Tech. Rep., Cold Regions Research & Engineering Laboratory, 1996.
- [67] R.A. Brown, “Longitudinal instabilities and secondary flows in the planetary boundary layer: A review,” *Review of Geophysics*, vol. 18, no. 3, pp. 683 – 697, 1980.

- [68] E.O. Nilsson, A. Rutgersson, A.-S. Smedman, and P.P. Sullivan, “Convective boundary-layer structure in the presence of wind-following swell,” *Quarterly Journal of the Royal Meteorological Society*, vol. 138, no. 667, pp. 1476–1489, 2012.
- [69] Y. Zhang and W. Perrie, “Feedback mechanisms for the atmosphere and ocean surface,” *Boundary-Layer Meteorology*, vol. 100, no. 2, pp. 321–348, 2001.
- [70] T.D. Sikora and S. Ufermann, *Synthetic Aperture Radar Marine User’s Manual*, chapter 14: Marine Atmospheric Boundary Layer Cellular Convection and Longitudinal Roll Vortices, pp. 321–330, U.S. Dept. of Commerce, NOAA, 2004.
- [71] I. Morrison, S. Businger, F. Marks, P. Dodge, and J.A. Businger, “An observational case for the prevalence of roll vortices in the hurricane boundary layer,” *Journal of the Atmospheric Sciences*, vol. 62, no. 8, pp. 2662–2673, 2005.
- [72] R.A. Brown, “On a satellite scatterometer as an anemometer,” *Journal of Geophysical Research*, vol. 88, no. C3, pp. 1663–1673, 1983.
- [73] T.M. Weckwerth, T.W. Horst, and J.W. Wilson, “An observational study of the evolution of horizontal convective rolls,” *Monthly Weather Review*, vol. 127, no. 9, pp. 2160–2179, 1999.
- [74] T.W. Gerling, “Structure of the surface wind field from the Seasat SAR.,” *Journal of Geophysical Research*, vol. 91, no. C2, pp. 2308–2320, 1986.
- [75] B. Brümmer, “Roll and cell convection in wintertime arctic cold-air outbreaks,” *Journal of the Atmospheric Sciences*, vol. 56, no. 15, pp. 2613–2636, 1999.
- [76] J.A. Zhang, K.B. Katsaros, P.G. Black, S. Lehner, J.R. French, and W.M. Drennan, “Effects of roll vortices on turbulent fluxes in the hurricane boundary layer,” *Boundary-Layer Meteorology*, vol. 128, no. 2, pp. 173–189, 2008.
- [77] W. Alpers and B. Brümmer, “Atmospheric boundary layer rolls observed by the synthetic aperture radar aboard the ERS-1 satellite,” *Journal of Geophysical Research*, vol. 99, no. C6, pp. 12613–12621, 1994.
- [78] R.C. Foster, “Why rolls are prevalent in the hurricane boundary layer,” *Journal of the Atmospheric Sciences*, vol. 62, no. 8, pp. 2647–2661, 2005.
- [79] S. Zecchetto and F. De Biasio, “Wind field retrieval from SAR images using the continuous wavelet transform,” in *International Geoscience and Remote Sensing Symposium (IGARSS)*, 2002, vol. 4, pp. 1974–1976.

- [80] A. Colling, Ed., *Ocean Circulation*, Butterworth-Heinemann & The Open University, 2nd edition, 2007.
- [81] T.M. Weckwerth, J.W. Wilson, R.M. Wakimoto, and N.A. Crook, “Horizontal convective rolls: Determining the environmental conditions supporting their existence and characteristics,” *Monthly Weather Review*, vol. 125, no. 4, pp. 505–526, 1997.
- [82] G. Levy, “Boundary layer roll statistics from SAR,” *Geophysical Research Letters*, vol. 28, no. 10, pp. 1993–1995, 2001.
- [83] W. Alpers and C. Melsheimer, *Synthetic Aperture Radar Marine User’s Manual*, chapter 17: Rainfall, pp. 355–371, U.S. Dept. of Commerce, NOAA, 2004.
- [84] A. Scoon and I. Robinson, “Meteorological and oceanographic surface roughness phenomena in the English Channel investigated using ERS synthetic aperture radar and an empirical model of backscatter,” *Journal of Geophysical Research C: Oceans*, vol. 105, no. C3, pp. 6469–6482, 2000.
- [85] F.M. Monaldo, D.R. Thompson, R.C. Beal, W.G. Pichel, and P. Clemente-Colón, “Comparison of SAR-derived wind speed with model predictions and ocean buoy measurements,” *IEEE Transactions on Geoscience and Remote Sensing*, vol. 39, no. 12, pp. 2587–2600, 2001.
- [86] C.B. Hasager, H.P. Frank, and B.R. Furevik, “On offshore wind energy mapping using satellite SAR,” *Canadian Journal of Remote Sensing*, vol. 28, no. 1, pp. 80–89, 2002.
- [87] F.M. Monaldo, D.R. Thompson, W.G. Pichel, and P. Clemente-Colón, “A systematic comparison of QuikSCAT and SAR ocean surface wind speeds,” *IEEE Transactions on Geoscience and Remote Sensing*, vol. 42, no. 2, pp. 283–291, 2004.
- [88] F. Fetterer, D. Gineris, and C.C. Wackerman, “Validating a scatterometer wind algorithm for ERS-1 SAR,” *IEEE Transactions on Geoscience and Remote Sensing*, vol. 36, no. 2, pp. 479–492, 1998.
- [89] W. Koch, “Directional analysis of SAR images aiming at wind direction,” *IEEE Transactions on Geoscience and Remote Sensing*, vol. 42, no. 4, pp. 702–710, 2004.
- [90] H. Shen, W. Perrie, and Y. He, “A new hurricane wind retrieval algorithm for SAR images,” *Geophysical Research Letters*, vol. 33, no. L21812, pp. 1–5, 2006.
- [91] J. Choisnard, D. Power, F. Davidson, B. Stone, C. Howell, and C. Randell, “Comparison of c-band SAR algorithms to derive surface wind vectors and initial findings in their use in marine search and rescue,” *Canadian Journal of Remote Sensing*, vol. 33, no. 1-4, pp. 1–11, 2007.

- [92] A.A. Mouche, F. Collard, B. Chapron, K.-F. Dagestad, G. Guitton, J.A. Johannessen, V. Kerbaol, and M.W. Hansen, “On the use of doppler shift for sea surface wind retrieval from SAR,” *IEEE Transactions on Geoscience and Remote Sensing*, vol. 50, no. 7, pp. 2901–2909, 2012.
- [93] C.M.H. Unal, P. Snoeij, and P.J.F. Swart, “The polarization-dependent relation between radar backscatter from the ocean surface and surface wind vector at frequencies between 1 and 18 GHz,” *IEEE Transactions on Geoscience and Remote Sensing*, vol. 29, no. 4, pp. 621–626, 1991.
- [94] D. R. Thompson, T. M. Elfouhaily, and B. Chapron, “Polarization ratio for microwave backscattering from the ocean surface at low to moderate incidence angles,” in *International Geoscience and Remote Sensing Symposium (IGARSS)*, 1998, vol. 3, pp. 1671–1673.
- [95] T. Elfouhaily, D.R. Thompson, D. Vandemarkt, and B. Chapron, “A new bistatic model for electromagnetic scattering from perfectly conducting random surfaces,” *Waves Random Media*, vol. 9, no. 3, pp. 281–294, 1999.
- [96] S. Lee, “The amundsen sea expedition 2012 (ANA02C), cruise report,” Tech. Rep., Korean Polar Research Institute, 2012.
- [97] S.D. Smith, “Coefficients for sea surface wind stress, heat flux, and wind profiles as a function of wind speed and temperature,” *Journal of Geophysical Research*, vol. 93, no. C12, pp. 15,467–15,472, 1988.
- [98] V.K. Makin, V.N. Kudryavtsev, and C. Mastenbroek, “Drag of the sea surface,” *Boundary-Layer Meteorology*, vol. 73, no. 1-2, pp. 159–182, 1995.
- [99] E.L. Andreas, “CRREL report 89-11: Thermal and size evolution of sea spray droplets,” Tech. Rep., U.S. Army Cold Regions Research and Engineering Laboratory, 1989.
- [100] O&SI SAF, *ASCAT Wind Product User Manual*, January 2010, version 1.8.
- [101] J. Verspeek, A. Stoffelen, M. Portabella, H. Bonekamp, C. Anderson, and J. F. Figa, “Validation and calibration of ASCAT using CMOD5,” *IEEE Trans. Geosci. Remote Sens.*, vol. 48, no. 1, pp. 386–395, 2010.
- [102] NCEP, “NCEP model analyses & forecasts,” 2010.
- [103] D. P. Dee, S. M. Uppala, A. J. Simmons, P. Berrisford, P. Poli, S. Kobayashi, U. Andrae, M. A. Balmaseda, G. Balsamo, P. Bauer, P. Bechtold, A. C. M. Beljaars, L. van de Berg, J. Bidlot, N. Bormann, C. Delsol, R. Dragani, M. Fuentes, A. J. Geer, L. Haimberger,

- S. B. Healy, H. Hersbach, E. V. Hólm, L. Isaksen, P. Kållberg, M. Köhler, M. Matricardi, A. P. McNally, B. M. Monge-Sanz, J.-J. Morcrette, B.-K. Park, C. Peubey, P. de Rosnay, C. Tavalato, J.-N. Thépaut, and F. Vitart, “The ERA-Interim reanalysis: configuration and performance of the data assimilation system,” *Quarterly Journal of the Royal Meteorological Society*, vol. 137, no. 656, pp. 553–597, 2011.
- [104] T.J. Bracegirdle and G.J. Marshall, “The reliability of antarctic tropospheric pressure and temperature in the latest global reanalyses,” *Journal of Climate*, vol. 25, no. 20, pp. 7138–7146, 2012.
- [105] S. Rahmstorf, “Ocean circulation and climate during the past 120,000 years,” *Nature*, vol. 419, no. 6903, pp. 207–214, 2002.
- [106] S. Jacobs, A. Jenkins, H. Hellmer, C. Giulivi, F. Nitsche, B. Huber, and R. Guerrero, “The Amundsen Sea and the Antarctic ice sheet,” *Oceanography*, vol. 25, no. 3, pp. 154–163, 2012.
- [107] H.D. Pritchard, S.R.M. Ligtenberg, H.A. Fricker, D.G. Vaughan, M.R. Van Den Broeke, and L. Padman, “Antarctic ice-sheet loss driven by basal melting of ice shelves,” *Nature*, vol. 484, no. 7395, pp. 502–505, 2012.
- [108] A. Shepherd, D.J. Wingham, J.A.D. Mansley, and H.F.J. Corr, “Inland thinning of pine island glacier, west antarctica,” *Science*, vol. 291, no. 5505, pp. 862–864, 2001.
- [109] A. Shepherd, D. Wingham, and E. Rignot, “Warm ocean is eroding west antarctic ice sheet,” *Geophysical Research Letters*, vol. 31, no. 23, pp. 1–4, 2004.
- [110] H.D. Pritchard, R.J. Arthern, D.G. Vaughan, and L.A. Edwards, “Extensive dynamic thinning on the margins of the greenland and antarctic ice sheets,” *Nature*, vol. 461, no. 7266, pp. 971–975, 2009.
- [111] S.S. Jacobs, A. Jenkins, C.F. Giulivi, and P. Dutrieux, “Stronger ocean circulation and increased melting under pine island glacier ice shelf,” *Nature Geoscience*, vol. 4, no. 8, pp. 519–523, 2011.
- [112] A.K. Wåhlin, R.D. Muench, L. Arneborg, G. Björk, H.K. Ha, S.H. Lee, and H. Alsén, “Some implications of ekman layer dynamics for cross-shelf exchange in the Amundsen Sea,” *Journal of Physical Oceanography*, vol. 42, no. 9, pp. 1461–1474, 2012.
- [113] D.P. Thoma, M.S. Moran, R. Bryant, M.M. Rahman, C.D.H. Collins, T.O. Keefer, R. Noriega, I. Osman, S.M. Skrivin, M.A. Tischler, D.D. Bosch, P.J. Starks, and C.D. Peters-Lidard, “Appropriate scale of soil moisture retrieval from high resolution radar

- imagery for bare and minimally vegetated soils,” *Remote Sensing of Environment*, vol. 112, no. 2, pp. 403–414, 2008.
- [114] E.J. Steig, Q. Ding, D.S. Battisti, and A. Jenkins, “Tropical forcing of circumpolar deep water inflow and outlet glacier thinning in the Amundsen Sea embayment, west Antarctica,” *Annals of Glaciology*, vol. 53, no. 60, pp. 19–28, 2012.
- [115] R.H. Stewart, *Introduction to Physical Oceanography*, Texas A&M University, 2008.
- [116] J.A. Polton, Y.-D. Lenn, S. Elipot, T.K. Chereskin, and J. Sprintall, “Can drake passage observations match ekman’s classic theory?,” *Journal of Physical Oceanography*, vol. 43, no. 8, pp. 1733–1740, 2013.
- [117] J. Marshall and R.A. Plumb, *Atmosphere, ocean and climate dynamics: An introductory text*, Elsevier Academic Press, 2008.
- [118] K.H. Mann and Lazier J.R., *Dynamics of Marine Ecosystems*, Blackwell Publishing, 3rd edition, 2006.
- [119] A.C. Naveira Garabato, K.L. Polzin, B.A. King, K.J. Heywood, and M. Visbeck, “Widespread intense turbulent mixing in the southern ocean,” *Science*, vol. 303, no. 5655, pp. 210–213, 2004.
- [120] P. Loubere, “The global climate system,” *Nature Education Knowledge*, vol. 3, no. 10, 2012.
- [121] W.S. Broecker, “The great ocean conveyor,” *Oceanography*, vol. 4, no. 2, pp. 79–89, 1991.
- [122] P.R. Pinet, *Invitation to Oceanography*, Jones and Bartlett Publishers, 5th edition, 2009.
- [123] K. Döös, J. Nilsson, J. Nycander, L. Brodeau, and M. Ballarotta, “The world ocean thermohaline circulation,” *Journal of Physical Oceanography*, vol. 42, no. 9, pp. 1445–1460, 2012.
- [124] S.R. Rintoul, *Earth System Monitoring: Selected Entries from the Encyclopedia of Sustainability Science and Technology*, chapter 10: Large-Scale Ocean Circulation: Deep Circulation and Meridional Overturning, pp. 199–232, Springer, 2013.
- [125] M. Thoma, A. Jenkins, D. Holland, and S. Jacobs, “Modelling circumpolar deep water intrusions on the Amundsen Sea continental shelf, Antarctica,” *Geophysical Research Letters*, vol. 35, no. L18602, pp. 1–6, 2008.

- [126] R. Pawlowicz, B. Beardsley, and S. Lentz, “Classical tidal harmonic analysis including error estimates in MATLAB using TDE,” *Computers and Geosciences*, vol. 28, no. 8, pp. 929–937, 2002.
- [127] R.E. Davis, “Predictability of sea level pressure anomalies over the North Pacific ocean,” *Journal of Physical Oceanography*, vol. 8, pp. 233–246, 1978.
- [128] P. Axe, “Oceanographic applications of coastal radar,” Tech. Rep. 41, SMHI, 2010.
- [129] P.E. La Violette, “The advection of submesoscale thermal features in the Alboran Sea gyre,” *Journal of Physical Oceanography*, vol. 14, no. 3, pp. 550–565, 1983.
- [130] A.C. Vastano and S.E. Borders, “Sea surface motion over an anticyclonic eddy on the Oyashio Front,” *Remote Sensing of Environment*, vol. 16, no. 1, pp. 87–90, 1984.
- [131] C.J. Koblinsky, J.J. Simpson, and T.D. Dickey, “An offshore eddy in the California current system part II: Surface manifestation,” *Progress in Oceanography*, vol. 13, no. 1, pp. 51–69, 1984.
- [132] J. Svejksky, “Sea surface flow estimation from Advanced Very High Resolution Radiometer and Coastal Zone Color Scanner satellite imagery: A verification study,” *Journal of Geophysical Research*, vol. 93, no. C6, pp. 6735–6743, 1988.
- [133] Ronald J. Holyer and Sarah H. Peckinpaugh, “Edge detection applied to satellite imagery of the oceans,” *IEEE Transactions on Geoscience and Remote Sensing*, vol. 27, no. 1, pp. 46–56, 1989.
- [134] A.K. Liu, C.Y. Peng, and S.Y.-S. Chang, “Wavelet analysis of satellite images for coastal watch,” *IEEE Journal of Oceanic Engineering*, vol. 22, no. 1, pp. 9–17, 1997.
- [135] W. J. Emery, A. C. Thomas, M. J. Collins, W. R. Crawford, and D. L. Mackas, “An objective method for computing advective surface velocities from sequential infrared satellite images,” *Journal of Geophysical Research: Oceans*, vol. 91, no. C11, pp. 12865–12878, 1986.
- [136] C.A.E. Garcia and I.S. Robinson, “Sea surface velocities in shallow seas extracted from sequential coastal zone color scanner satellite data,” *Journal of Geophysical Research*, vol. 94, no. C9, pp. 12681–12691, 1989.
- [137] M. Kamachi, “Advective surface velocities derived from sequential images for rotational flow field: limitations and applications of maximum cross correlation method with rotational registration,” *Journal of Geophysical Research*, vol. 94, no. C12, pp. 18227–18233, 1989.

- [138] R. Tokmakian, P.T. Strub, and J. McClean-Padman, "Evaluation of the maximum cross-correlation method of estimating sea surface velocities from sequential satellite images," *Journal of Atmospheric and Oceanic Technology*, vol. 7, pp. 852–865, 1990.
- [139] W.J. Emery, C. Fowler, and C.A. Clayson, "Satellite-image-derived gulf stream currents compared with numerical model results," *Journal of Atmospheric & Oceanic Technology*, vol. 9, no. 3, pp. 286–304, 1992.
- [140] James A. Holland and Xiao-Hai Yan, "Ocean thermal feature recognition, discrimination, and tracking using infrared satellite imagery," *IEEE Transactions on Geoscience and Remote Sensing*, vol. 30, no. 5, pp. 1046–1053, 1992.
- [141] Qing X. Wu, David Pairman, Stephen J. McNeill, and Edward J. Barnes, "Computing advective velocities from satellite images of sea surface temperature," *IEEE Transactions on Geoscience and Remote Sensing*, vol. 30, no. 1, pp. 166–176, 1992.
- [142] Q. X. Wu, "A correlation-relaxation-labeling framework for computing optical flow - template matching from a new perspective," *IEEE Transactions on Pattern Analysis and Machine Intelligence*, vol. 17, no. 8, pp. 843–853, 1995.
- [143] G. Borzelli, G. Manzella, S. Marullo, and R. Santoleri, "Observations of coastal filaments in the Adriatic Sea," *Journal of Marine Systems*, vol. 20, no. 1-4, pp. 187–203, 1999.
- [144] C.M. Domingues, G.A. Gonçalves, R.D. Ghisolfi, and C.A.E. Garcia, "Advective surface velocities derived from sequential infrared images in the southwestern atlantic ocean," *Remote Sensing of Environment*, vol. 73, no. 2, pp. 218–226, 2000.
- [145] J.S. Prasad, A.S. Rajawat, Y. Pradhan, O.S. Chauhan, and S.R. Nayak, "Retrieval of sea surface velocities using sequential Ocean Colour Monitor (OCM) data," *Proceedings of the Indian Academy of Sciences, Earth and Planetary Sciences*, vol. 111, no. 3, pp. 189–195, 2002.
- [146] M.M. Bowen, W.J. Emery, J.L. Wilkin, P.C. Tildesley, I.J. Barton, and Rebecca Knewtson R., "Extracting multiyear surface currents from sequential thermal imagery using the maximum cross-correlation technique," *Journal of Atmospheric and Oceanic Technology*, vol. 19, no. 10, pp. 1665–1676, 2002.
- [147] S. Dransfeld, G. Larnicol, and P.-Y. Le Traon, "The potential of the maximum cross-correlation technique to estimate surface currents from thermal avhrr global area coverage data," *IEEE Geoscience and Remote Sensing Letters*, vol. 3, no. 4, pp. 508–511, 2006.

- [148] R.I. Crocker, D.K. Matthews, W.J. Emery, and D.G. Baldwin, “Computing coastal ocean surface currents from infrared and ocean color satellite imagery,” *IEEE Transactions on Geoscience and Remote Sensing*, vol. 45, no. 2, pp. 435–447, 2007.
- [149] J. Marcello, F. Eugenio, F. Marqués, A. Hernández-Guerra, and A. Gasull, “Motion estimation techniques to automatically track oceanographic thermal structures in multi-sensor image sequences,” *IEEE Transactions on Geoscience and Remote Sensing*, vol. 46, no. 9, pp. 2743–2762, 2008.
- [150] E.M. Armstrong, G. Wagner, J. Vazquez-Cuervo, and T.M. Chin, “Comparisons of regional satellite sea surface temperature gradients derived from MODIS and AVHRR sensors,” *International Journal of Remote Sensing*, vol. 33, no. 21, pp. 6639–6651, 2012.
- [151] P. Castellanos, J.L. Pelegr, D. Baldwin, W.J. Emery, and A. Hernández-Guerra, “Winter and spring surface velocity fields in the cape blanc region as deduced with the maximum cross-correlation technique,” *International Journal of Remote Sensing*, vol. 34, no. 9-10, pp. 3587–3606, 2013.
- [152] K. Masuda, T. Takashima, and Y. Takayama, “Emissivity of pure and sea waters for the model sea surface in the infrared window regions,” *Remote Sensing of Environment*, vol. 24, no. 2, pp. 313–329, 1988.
- [153] D.D. Wahl and J.J. Simpson, “Physical processes affecting the objective determination of near-surface velocity from satellite data,” *Journal of Geophysical Research*, vol. 95, no. C8, pp. 13511–13528, 1990.
- [154] NOAA, “NOAA KLM user’s guide,” 2009.
- [155] L. Funkquist and E. Kleine, “An introduction to HIROMB, an operational baroclinic model for the baltic sea,” Report Oceanography 37, Swedish Meteorological and Hydrological Institute (SMHI), 2007.